Journal of Non-Newtonian Fluid Mechanics 282 (2020) 104293

Contents lists available at ScienceDirect

Journal of Non-Newtonian Fluid Mechanics

journal homepage: www.elsevier.com/locate/jnnfm

Electro-elastic flow instabilities of viscoelastic fluids in contraction/expansion micro-geometries

Samir H. Sadek[a], Fernando T. Pinho[a], Manuel A. Alves[b,*]

[a] CEFT, Departamento de Engenharia Mecânica, Faculdade de Engenharia da Universidade do Porto, Rua Dr. Roberto Frias, 4200-465 Porto, Portugal
[b] CEFT, Departamento de Engenharia Química, Faculdade de Engenharia da Universidade do Porto, Rua Dr. Roberto Frias, 4200-465 Porto, Portugal

ARTICLE INFO

Keywords:
Electro-osmotic flow (EOF)
Electro-elastic instabilities (EEI)
Contraction/expansion micro-geometries
Viscoelastic fluids
Newtonian fluids

ABSTRACT

Electro-elastic instabilities in electro-osmotic contraction/expansion flows (EOF) of viscoelastic fluids are experimentally investigated in this work. Several microchannel configurations are used, including the cases with hyperbolic-shaped contractions followed by an abrupt expansion, or abrupt contractions followed by a hyperbolic-shaped expansion. Such cases were selected to assist in the understanding of the EOF instability mechanisms and at which conditions they occur. A reference Newtonian fluid was also used in the experiments, and a wide range of electric fields were imposed to drive the flow. Flow visualizations for a Newtonian fluid allowed to assess the impact of dielectrophoresis on the velocity field of the seeding particles. For each geometry, depending on the polymer concentration, the flow was found to be quasi-Newtonian below a critical electric potential difference, characterized by smooth parallel steady flow patterns in the upstream and downstream channels. Above the critical voltage difference two types of electro-elastic instabilities were found to occur, leading to an unsteady symmetric flow, and to time-dependent irregular flow.

1. Introduction

Efficient mixing is essential to enhance the performance of micro-scale devices, as found in many pharmacological, clinical and diagnostic analyses which rely on small samples where fast and complete reactions are needed [1]. Mixing is usually difficult in microchannel flows, because at the low Reynolds numbers typical of laminar flow the process is limited by molecular diffusion, thus flow instabilities are welcome to overcome this limitation. Simultaneously, electro-kinetic flow forcing methods are particularly suitable for miniaturization and are increasingly used in micro-scale devices. Recently, electro-osmosis (EO) driven flows have been used to enhance micro-scale mixing through flow instabilities [2–4] triggered either by electro-kinetic instabilities (EKIs), commonly found for Newtonian fluid flows [5–9], or through electro-elastic instabilities (EEIs) using viscoelastic fluids [2–4].

Classical EKIs occur when high intensity external electrical fields [5–9] are applied to drive flows of fluids with significantly different electrical conductivities. EKIs occur with different fluids, including Newtonian fluids, as long as there are large conductivity gradients, but EKIs are beyond the scope of this work. In contrast EEIs occur with viscoelastic fluids, which are able to develop elastic instabilities in the presence of electro-kinetic forcing. The main objective of this work is to investigate EEIs in viscoelastic fluids.

Miniaturization reduces the characteristic length and time scales of the flow, thus enhancing the effects of fluid elasticity, which vary inversely with the square of the characteristic length scale. The inherent elastic nonlinearities [10] drive elastic instabilities that can be used to promote mixing, as with inertial turbulence at macro-scale flows. Elastic instabilities in microfluidic flows of viscoelastic fluids have been frequently observed in pressure driven flows (PDF) [10–14], but also in EO driven flows [2–4], provided the flow velocities achieved are sufficiently high to drive elastic instabilities. Both cases are reviewed next, starting with PDFs.

The transition from stable to unstable laminar flow due to fluid elasticity in PDF depends on flow topology, in particular on the occurrence of curved streamlines, on the Reynolds and Weissenberg numbers and on other dimensionless numbers associated with fluid rheology. Specifically, there can be a direct transition from steady symmetric to time-dependent flow, or alternatively the onset of two purely elastic flow instabilities, including the transition from a steady symmetric to a steady asymmetric flow, and the subsequent transition to time-dependent flow at higher Weissenberg numbers [10–14]. This latter path of transitions was reported experimentally for PDF by Arratia et al. [11] using a cross-slot flow geometry (i.e. a configuration with two orthogonal flow inlets and two outlets), and later predicted numerically by Poole et al. [10] for creeping flows of viscoelastic fluids described by the upper-convected

Abbreviations: EDL, Electric double layer; EO, Electro-osmosis; EKI, Electro-kinetic instabilities; PDF, Pressure-driven flows; PTV, Particle tracking velocimetry.

* Corresponding author.
E-mail address: mmalves@fe.up.pt (M.A. Alves).

https://doi.org/10.1016/j.jnnfm.2020.104293
Received 31 July 2019; Received in revised form 8 April 2020; Accepted 12 April 2020
Available online 11 May 2020

Maxwell model. Even though both works ([10] and [11]) only agreed qualitatively, both found a critical Deborah number (*De*) that characterizes the first type of transition (between steady states), and subsequently the second higher critical *De* in which the steady asymmetric flow eventually became time-dependent. Similar observations were also reported in [12–14] for viscoelastic fluid flow in a flow-focusing device, i.e. a configuration with three orthogonal flow inlets and one outlet, and in other geometries with curved streamlines.

Whereas in pressure-driven flows shear effects are present everywhere in the flow field, and more intensively near the channel walls, in electro-osmotic flows (EOF) shear effects are mostly confined to the thin electric double layers (EDL) at the walls [15]. This can be an advantage in situations where micro-mixing is undesirable, as in micro-rheology chips (devices to measure the rheological properties of fluids). However, the very thin EDL also leads locally to very high velocity gradients, even if the velocity outside the EDL is not large. The EO driven flows may also exhibit peculiar elastic flow transitions akin to those found in PDF and the main goal of this work is to investigate the characteristics of EEIs in EO driven flows.

Bryce and Freeman [3,4] were among the first to report the existence of EEIs. They found that by forcing a polymer-free solution through a linear microchannel with sudden 2:1 constrictions leads to a stable laminar creeping flow, whereas by adding a small amount of high molecular weight polymer mixture, which imparted elasticity to the solution, results on the appearance of large flow instabilities and enhanced mixing. Although shear was mainly limited to the EDL, flow instabilities occurring in the microchannel streamwise direction were due to the presence of polymer molecules in the bulk flow and found to comply with the Pakdel-McKinley mechanism [16], where elastic normal stresses developing along curved streamlines make it unstable when they exceed by a certain amount the local shear stress, thereby breaking the stability of laminar flow. Hence, they found that flow instabilities were enhanced in regions of curved streamlines in contrast to polymer-free solutions which continuously displayed stable flow under the range of electric potentials investigated.

Bryce and Freeman [4] used the same sudden constriction flow configuration as in [3], but the focus was on understanding the underlying extensional nature of the flows. They arrived at similar conclusions as for shear flow namely that elastic instabilities appeared when the flow rate reached a critical value, even for dilute polymer solutions. The measured flow fluctuations associated with the instabilities quickly increased to a peak value during the transition between states and became nearly constant for post-critical conditions. In addition, micro-gel formation was observed when applying a high voltage difference between the electrodes. The authors also found that polymer addition, on one hand, decreased slightly flow mixing due to enhanced viscosity, but on the other hand it increased fluid elasticity, which generated stronger elastic instabilities [3,4] that enhanced mixing.

These experimental findings inspired the early numerical investigations of Afonso et al. [2] of EOF in the reference cross-slot flow geometry with fluids described by the upper-convected Maxwell and the simplified Phan-Thien–Tanner models. They were able to predict an elastic instability from steady symmetric to unsteady flow at a critical *Wi,* which correlated well with the strong velocity gradients within the EDL region through the Pakdel-McKinley criterion, so that reducing the EDL thickness decreased the value of the critical Weissenberg number (*Wi*). They argued that the absence of the transition from steady symmetric to steady asymmetric flow, could be due to the fact that for pure EOF shear effects are limited to the wall/corner EDLs, hence the EOF becomes less capable to sustain the steady asymmetric flow in the cross-slot geometry.

Recently, Ko et al. [17] investigated experimentally EOF in a constriction microchannel, for a wide range of imposed direct current (DC) potential differences. Four different types of non-Newtonian polymeric solutions (polyacrylamide (PAA), polyethylene oxide (PEO), xanthan gum (XG), polyvinylpyrrolidone (PVP)) were used to assess the influence of their rheological characteristics on the flow behavior upstream and downstream of the channel constriction. In their experiments, PVP and PEO behaved in a Newtonian-like way arguably on account of their weakly shear-thinning behavior, while for the shear-thinning solution of XG multiple pairs of flow recirculations were formed, which were absent in the strongly elastic and shear thinning PAA solution flows.

There is still limited experimental information in the literature regarding EEIs, which this work aims to address. Here, we investigate experimentally the flow behavior of viscoelastic fluids in microchannels with hyperbolic shaped contractions and focus on studying electro-elastic instabilities in electro-osmotic driven flows. The conditions under which instabilities may occur are investigated in four different geometrical configurations (described in Section 2.1), using a reference Newtonian fluid and four different aqueous solutions of polyacrylamide (M_w=5 × 10^6 g mol^{-1}) at weight concentrations of 100, 300, 1000 and 10000 ppm (their rheological characterization is presented in Section 2.2) and under a wide range of imposed electric potential differences. For pressure-driven flow, these geometrical flow configurations exhibit flow instabilities as previously investigated by others, such as Campo-Deaño et al. [18] and Sousa et al. [19]. In the former work, a microchannel with a hyperbolic contraction followed by an abrupt expansion was used to characterize the degree of elasticity of low viscosity Boger fluids: the critical conditions for the onset of elastic instabilities were used to quantify the relaxation time of low concentration polymeric solutions, with the length of the upstream corner vortices being used as indicators of the degree of elasticity.

Flow visualization and particle tracking velocimetry (PTV) are the experimental techniques used and they are briefly described in Section 2.3. Additionally, a numerical viscoelastic EOF solver, entitled *RheoTool*, was used to predict the Newtonian flow behavior in a certain number of flow configurations to help clarify and understand its flow dynamics. *RheoTool* is an open-source toolbox solver developed by Pimenta and Alves [20], and is based on the open source OpenFOAM® toolbox, which is available for download at the following GitHub repository: https://github.com/fppimenta/rheoTool. More details specific of electro-osmotic flows using *RheoTool* can be found in Pimenta and Alves [21].

2. Experimental set-up

2.1. Microchannel geometry and fabrication

Two microchannels with a contraction were used, denoted here H_2 and H_3 (the subscript denotes the Hencky strain) and each device can be used in the forward (-f) and backward (-b) flow configurations. In the first two configurations of Figs. 1-(A) and (B), flow is from left to right through a hyperbolic contraction followed by an abrupt expansion, which we denote as the forward direction. By inverting the electrode polarity flow will be from right to left, in the corresponding backward configurations of Figs. 1-(C) and (D).

The relevant *design* dimensions of the microchannels are presented in Fig. 1-(E) and Table 1. The microchannels were designed to have Hencky strains $\epsilon_H = \ln(w_1/w_2) = 2$ or 3. The upstream width is always w_1 = 400 μm, the contraction minimum widths are w_2 = 54.1 or 19.9 μm, and the contraction lengths are L_c = 128 or 382 μm, respectively (Table 1). All microchannels were designed to have a constant depth, H = 100 μm and equal upstream (L_u) and downstream (L_d) lengths of 4 mm, but the final measured real dimensions of the PDMS microchannels differ slightly, so they are also included in Table 1. The total length of the microchannel is defined as $L_{total} = L_u + L_c + L_d$, and is presented in Table 1. All PDMS microchannels are made from the same mold and reproducibility is quite good as previously assessed extensively by Oliveira et al. [22], with depths having a variation of about ±1 μm.

The hyperbolic shape is used to impose a nearly constant extension rate along the centerline of the microchannel [22], as can be theoretically demonstrated from the assumption of plug flow, which is a good

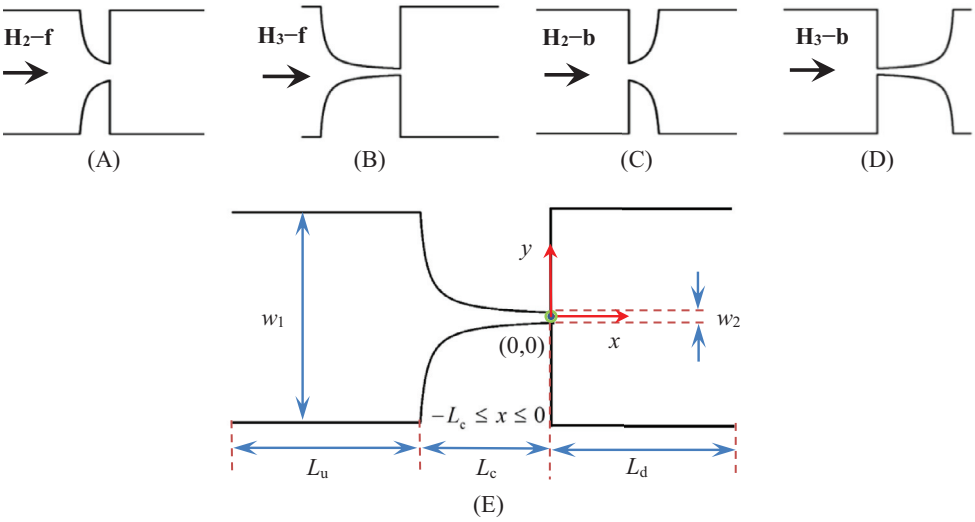

Fig. 1. Schematic representation of microchannels H_2 ($\epsilon_H = 2$) and H_3 ($\epsilon_H = 3$): microchannels (A) and (B) have a hyperbolic contraction followed by an abrupt expansion; microchannels (C) and (D) have an abrupt contraction followed by a hyperbolic expansion; part (E) represents the relevant dimensions of the microchannels. The black arrows indicate the flow direction. The origin of the Cartesian coordinate system is located at the centerline with the z-coordinate measured from the bottom wall.

Table 1
Microchannels dimensions, including the design and the real dimensions.

Microchannel configuration	Hencky strain (ϵ_H)	Design dimensions (μm)					Microchannel dimensions (μm)						
		w_1	w_2	L_c	H	w_1/w_2	w_1	w_2	L_c	H	D_h	w_1/w_2	L_{total}
Contraction-expansion: H_2, see Fig. 1-(A)	2	400	54.0	128	100	7.4	401	56	127	94	70	7.2	8130
Contraction-expansion: H_3, see Fig. 1-(B)	3	400	19.9	382	100	20.1	403	18	383	92	30	22.4	8380

estimate for electro-osmotic flows. The origin of the Cartesian coordinate system is at the centerline, at the sudden contraction/expansion plane (the z-coordinate is measured from the bottom wall) as shown in Fig. 1-(E). Thus, the channel upper and lower upstream walls of the hyperbolic shaped microchannel obey the following profile [18,19]:

$$y = \pm(w_1/2)/\left[1 + 0.05(x + L_c)\right] \text{ valid for } -L_c \le x \le 0 \quad (1)$$

Eq. (1) applies to both microchannels H_2 and H_3, with all dimensions given in μm.

The microchannels were fabricated in polydimethylsiloxane (PDMS; Sylgard 184, Dow Corning Inc) using SU-8 photoresist molds. The ratio of 5:1 (wt/wt) of PDMS to curing agent was used to fabricate the microchannels.

In the experimental setup two platinum electrodes were used, each one mounted at the microchannel inlet and outlet terminals, respectively. The fluid reservoirs at the microchannel inlet and outlet were maintained at the same level through an external connection in order to avoid the build-up of an adverse pressure gradient due to EO flow. In this system, the fluid driven by EO into the downstream reservoir is externally reintroduced by gravity in the upstream reservoir, allowing the system to operate continuously without generating an adverse pressure gradient.

2.2. Rheological characterization of the fluids

A total of five solutions were used, including one Newtonian and four viscoelastic fluids. The working solutions were seeded with fluorescent polystyrene particles (FluoSpheres® Carboxylate-Modified Microspheres, Nile Red, Molecular Probes®) with an average diameter of 1 μm, at a concentration of 24 ppm (wt/wt). The Newtonian fluid used was an aqueous solution of 1 mM borate buffer (Sigma-Aldrich), with 0.05% (wt/wt) of sodiumdodecylsulfate (SDS, Sigma-Aldrich) added to reduce particle adhesion to the microchannel walls. A small amount of fluorescent dye (Rhodamine B, Sigma-Aldrich) was also added to enhance the contrast and light intensity of the tracer particles, unless otherwise stated. The viscoelastic fluids were four aqueous solutions of polyacrylamide (Polysciences), with concentrations of 100, 300, 1000 and 10000 ppm (wt/wt). The PAA mother solution used had a molecular weight of $M_w = 5 \times 10^6$ g mol^{-1} and was directly dissolved in distilled water, without the addition of SDS or fluorescent dye, unless otherwise stated.

The characterization of all fluids included the measurement of the solution conductivity (conductivity meter CDB-387, Omega) and the solution pH (pH meter model pH 1000L from pHenomenal®, VWR probe/device). For the viscoelastic PAA fluids, the characterization also included measurements of the shear and extensional rheology. The shear-thinning viscosity in steady shear flow was measured using a rotational rheometer (Physica MCR301, Anton Paar) with a 75 mm diameter cone-plate system with 1° angle, and the extensional relaxation time λ was measured using a capillary-breakup extensional rheometer [23], which allows reliable measurements of the extensional relaxation time of dilute polymer solutions down to about 100 μs. Electric-related data for all fluids as well as the extensional relaxation time of the viscoelastic solutions can be found in Table 2, whereas the viscosity curves for all fluids are plotted in Fig. 2. No reliable measurements of first normal stress difference in shear could be obtained for any of the polymer solutions due to their low polymer concentrations. The relaxation time in Table 2 is obtained by averaging three measured values for each polymer concentration, and based on the three measurements, the computed standard deviation is 0.14, 0.02, 0.22 and 0.1 ms for the 100, 300, 1000 and 10000 ppm, respectively.

The shear viscosity for the 100 ppm solution is essentially that of the water solvent at the same temperature (0.00097 Pa.s), and for the 300 and 1000 ppm solutions the viscosity is essentially constant at 0.00118 and 0.0018 Pa.s, respectively. For the 10000 ppm polymer solution we fitted a simplified Carreau-Yasuda model $\eta = \eta_\infty + (\eta_0 - \eta_\infty)[1 + (\lambda_Y\dot{\gamma})^a]^{(n-1)/a}$ with coefficients $\eta_0 = 0.0542$ Pa.s, $\eta_\infty = 0.00097$ Pa.s, $a = 1.18$, $\lambda_Y = 0.0206$ s, and $n = 0.624$. This fitted equation is included in Fig. 2.

2.3. Experimental methods and procedures

The experiments were conducted by imposing an electric field using a DC power supply (EA-PS 5200-02 A, EA-Elektro-Automatik-GmbH). The microchannels were placed on the stage of an inverted epi-fluorescence microscope (Leica Microsystems GmbH, DMI 5000M),

Table 2
Electrical conductivity and pH of the working solutions and extensional relaxation time of viscoelastic fluids, measured at T = 295 K.

	Borate buffer 1.0 mM (using 0.05% SDS)		Solution concentration of PAA (ppm) (Without dye or SDS)			
	With dye	Without dye	100	300	1000	10000
pH	9.1	9.1	6.1	6.3	6.6	7.7
Electrical conductivity (μS/cm)	265	263	20.2	55.5	178.3	161.8
Relaxation time, λ (ms)	-	-	0.36	0.59	1.7	6.3

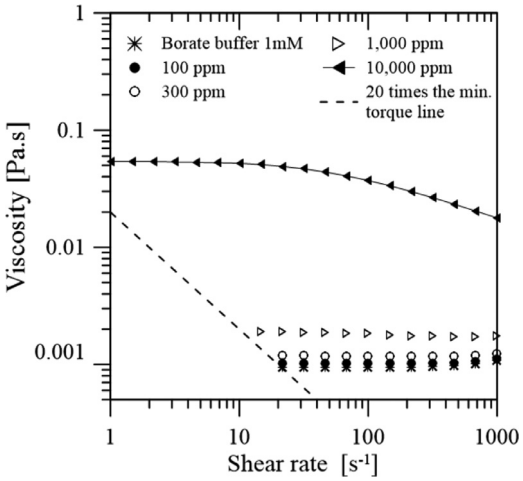

Fig. 2. Shear viscosity curves in steady shear flow for all fluids at T = 295 K. The solid line represents the fit of the 10000 ppm data by the Carreau-Yasuda model.

equipped with a continuous light source (100W mercury lamp), a filter cube (Semrock CY3-4040C), and either a 20X objective (Leica Microsystems GmbH, numerical aperture NA = 0.4), or a 10X objective (Leica Microsystems GmbH, numerical aperture NA = 0.3). Two cameras were coupled to the microscope to characterize the flow behavior, one for flow visualization, and the other for the PTV measurements.

The flow visualizations were carried out using a long exposure streak imaging technique which required a camera with a sensor that can operate with *long* exposure times with low noise. We used an Andor Neo 5.5 sCMOS camera, controlled using μ-Manager software (v.1.4.19) together with a 10X objective. The camera was set to acquire 20 frames per run, using its full-resolution (2560 × 2160 pixels; each pixel corresponds to 0.407 μm x 0.407 μm in our setup), and an exposure time varying according to the flow rate, between 1.0 and 15.0 s (lower exposure time for higher flow rates and vice-versa).

The PTV technique requires the use of a high-speed camera, that can acquire a large number of successive frames. Unless otherwise stated, this was achieved with the Photron FASTCAM Mini UX100 high-speed camera operating with the 20X objective and set to acquire 1000 frames per second (fps) for each run, at full-resolution (1280 × 1024 pixels; each pixel has 0.498 μm x 0.498 μm in the setup used). The PTV algorithm used to compute the displacement of the particles and corresponding velocity comprises two consecutive steps. The first step starts by using an open source image processing program, ImageJ software (version 1.51j8, www.imagej.net/), in combination with the open source particle tracking plugin MOSAIC to identify and scan a specified number of successive frames for each possible bright spot corresponding to individual in-focus fluorescent tracer particles in the flow field [24]. The frames were recorded over the maximum camera recording time, which is dictated by the available RAM memory of the camera (8 GB in each run), and typically consists of about 4365 frames at full resolution. The second step involves the use of a Matlab® code (MathWorks, version R2012a) for data post-processing. Subsequently the displacements of the particles and the corresponding velocities were computed. All experiments were carried out at T=295 K.

3. Results and discussion

The Newtonian fluid provides the reference flow characteristics for each of the geometries investigated. For viscoelastic fluids we varied the applied voltage from low values, corresponding to stable flow, up to high voltages that lead to unstable flow conditions. We present first the results for the Newtonian solution followed by the viscoelastic fluid results, preceded by a description of the relevant dimensionless numbers.

3.1. Relevant dimensionless numbers

To differentiate between microchannels with the same geometrical configuration, a dimensionless kinematic number known as Hencky strain (ε_H) was used in Section 2.1, but additional dimensionless numbers are required to fully characterize the flow. To assess whether a flow is dominated by inertial or viscous forces, the Reynolds number (Re) is used, here defined as [25]:

$$Re = \rho D_h u_2/\mu \tag{2}$$

where D_h=2$Hw_2/(H+w_2)$ is the hydraulic diameter based on the microchannel real dimensions (see Table 1), u_2 is the maximum velocity at the throat minimum width w_2, ρ is the fluid density (assumed constant), and μ is the characteristic shear viscosity of the fluid, determined at the characteristic shear rate $\dot{\gamma}_2$=$u_2/(w_2/2)$ for the viscoelastic fluids.

To characterize the flow elasticity of the PAA solutions at least one additional dimensionless parameter is required, typically, the Deborah number (De), which is defined as the ratio between the relaxation time of the fluid (λ) and the characteristic time scale of the flow, $(w_2/2)/u_2$ [26,27]:

$$De = 2\lambda u_2/w_2 \tag{3}$$

The Weissenberg number (Wi) may also be used to quantify elastic effects for the hyperbolic contraction, and is given by [25]:

$$Wi = \lambda(u_2 - u_1)/L_c = \lambda\dot{\epsilon} \tag{4}$$

where u_1 is the bulk average velocity at the upstream microchannel of width w_1, L_c is the hyperbolic contraction length (see Fig. 1-(E) and Table 1) and $\dot{\epsilon}$ is the average extension rate along the centerline of the hyperbolic contraction region.

The use of either the Deborah or the Weissenberg number depends on the physical phenomena under study. The Deborah number is more appropriate to describe non-homogeneous flows that have a variable stretch history, whereas Wi is more suitable for steady homogeneous flows with constant stretch history [28]. Thus, Wi will be used for the flows through the hyperbolic shaped microchannels under investigation, which are expected to have a nearly constant extension rate along the contraction centerline.

3.2. Newtonian fluid

3.2.1. Flow visualization

Flow visualizations were carried out by adjusting the focus of the 10X objective at the microchannel mid-plane (at mid-distance between the top and bottom walls in the z-direction, see Fig. 1-(E)).

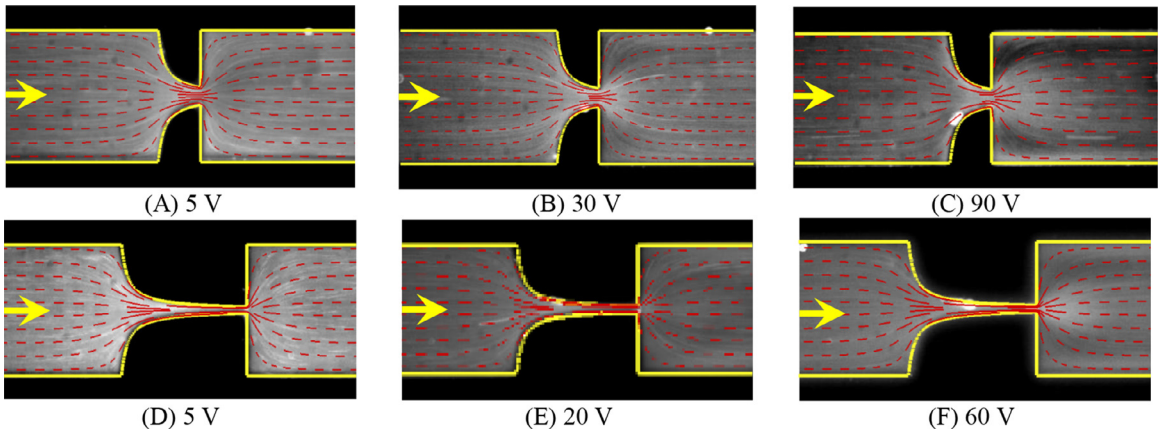

Fig. 3. Flow visualizations in microchannel H_2−f (A, B and C) at ΔV = 5, 30 and 90V, and in microchannel H_3−f (D, E and F) at ΔV=5, 20 and 60V, using the 1 mM borate buffer with dye. The red dashed lines represent the numerically predicted streamlines for a purely electro-osmotic flow of a Newtonian fluid, and the yellow lines are used to highlight the microchannel walls. The yellow arrows indicate the flow direction. The Reynolds number computed at the throat for microchannels H_2−f, and H_3−f are 0.13 (90V) and 0.084 (60V), respectively, at the highest voltages. (For interpretation of the references to color in this figure legend, the reader is referred to the web version of this article.)

Flow visualizations for the Newtonian fluid, are presented in Fig. 3 for microchannels H_2−f and H_3−f, both in the forward flow configurations (cf. Fig. 1-(A) and (B)). The effect of ΔV on the flow field was assessed and each plot presents also the corresponding streamlines predicted numerically, shown as red dashed lines, by assuming a steady two-dimensional (2D) pure EO driven flow of a Newtonian fluid. The experimental pathlines are the imaged white traces obtained using the streak photography technique. By combining in the same image the numerically predicted 2D streamlines with the experimental flow patterns, we observe that there is no qualitative influence of dielectrophoresis acting on the seeding particles upon the flow patterns due to electro-osmosis. The flow patterns for microchannel H_2−f are under ΔV=5, 30 and 90 V, whereas for microchannel H_3−f, ΔV=5, 20 and 60 V. Since the Reynolds numbers at the throat are small (maximum *Re* of 0.13 and 0.084 for H_2−f and H_3−f, respectively) as expected, the observed flow patterns in all cases are typically laminar without separated flow regions appearing downstream of the expansion, even at the highest imposed potential difference. Micro-particles tend to stick to walls, usually appearing at high flow rates, and tend to accumulate in narrow passages, appearing in the images as bright spots, and the maximum imposed DC potential that could be used, without blocking the microchannel, was around 90 V for microchannels H_2−f, and 60 V for microchannels H_3−f. Flow visualizations for the corresponding backward flow configurations H_2−b and H_3−b (cf. Fig. 1-(C) and (D)) were not carried out, but similar well-behaved laminar attached flow behavior is expected, at such small *Re*.

In summary, the Newtonian flow is dominated by viscous forces and the fluid is able to negotiate even the sharp geometric features without flow separation. Since the numerically predicted streamlines and the recorded experimental pathlines are nearly identical, as shown in Fig. 3, we conclude that dielectrophoresis has a negligible influence on the seeding particles qualitative behavior and consequently on the electro-osmotic flow streamlines. We note that particles are also subjected to electrophoresis (EP), as discussed in [29] and that for Newtonian (viscous) fluids in the linear regime, the expected electrophoretic and electro-osmotic velocity fields are co-linear, thus the expected streamlines for EO and EP are the same.

3.2.2. *Measurements of the centerline velocity*

Using the PTV technique, the centerline velocity was measured in a window located at the microchannel mid-plane around the centerline, with a deviation of ± 1.25 % of the microchannel upstream width ($y = \pm 0.0125\, w_1$). This is typically the region where all tracer particles move parallel to the microchannel centerline, i.e., where the velocity component in the *y*-direction is negligible. Accordingly, for averaging purposes the centerline of the microchannel was divided into several equally-spaced segments along the microchannel *x*-direction, each about 5 pixels long. Then, the tracer particles velocity components within each segment were averaged to obtain the corresponding segment average-velocity, and the corresponding velocity profile along the microchannel centerline.

Before measuring the centerline velocity at the microchannel mid-plane, and to perform accurate measurements of the centerline velocity, it is worth to investigate several technical settings, such as: *i*) how to carefully define the edges of the hyperbolic PDMS contraction walls, especially in the throat region; *ii*) how the centerline velocity varies with depth (*z*), numerically and experimentally; *iii*) how the use of dye may improve the image quality, while possibly having a significant side effect on the measured velocity. Each of these issues are discussed at length in Appendices A, B and C, respectively.

In the Newtonian PTV experiments, 1 μm tracer particles were used. As understood from the appendices, the best setting used combines a depth of z/H = 0.15 (chosen as the default measuring depth for all subsequent measurements with Newtonian fluid), with a small amount of fluorescent dye (mainly added to improve image quality), and a 20X objective. A high-speed camera was also used, unless otherwise stated.

Fig. 4 presents centerline velocity profiles measured in microchannels H_2-f and H_3-f, for imposed ΔV between 5 and 90V. As expected, the hyperbolic shape imposes nearly constant extensional strain rates (corresponding to linear velocity profiles) along the centerline of the microchannels, even at high ΔV, as shown in Fig. 4-(B) and (D). These plots also show a comparable behavior between the measured normalized velocity profiles and those of the numerical simulations. Each experiment was repeated once to assess the repeatability under the same operating conditions, and accordingly each figure may use two or more of the following abbreviations to refer to the successive number of experimental runs: R1 and R2. Note that each run was done in a new microchannel. A slight difference in the velocity profiles is observed between the first and second runs for microchannel H_3, see Fig. 4-(D), which may be due to the hyperbolic walls having some possible slight defects created during the PDMS fabrication, or due to some tracer particle accumulation on the hyperbolic walls.

Fig. 5 plots the velocity at the center of the upstream channel (u_1) and at the throat of the contraction (u_2) for microchannels H_2−f and H_3−f as a function of the imposed potential difference. As expected for

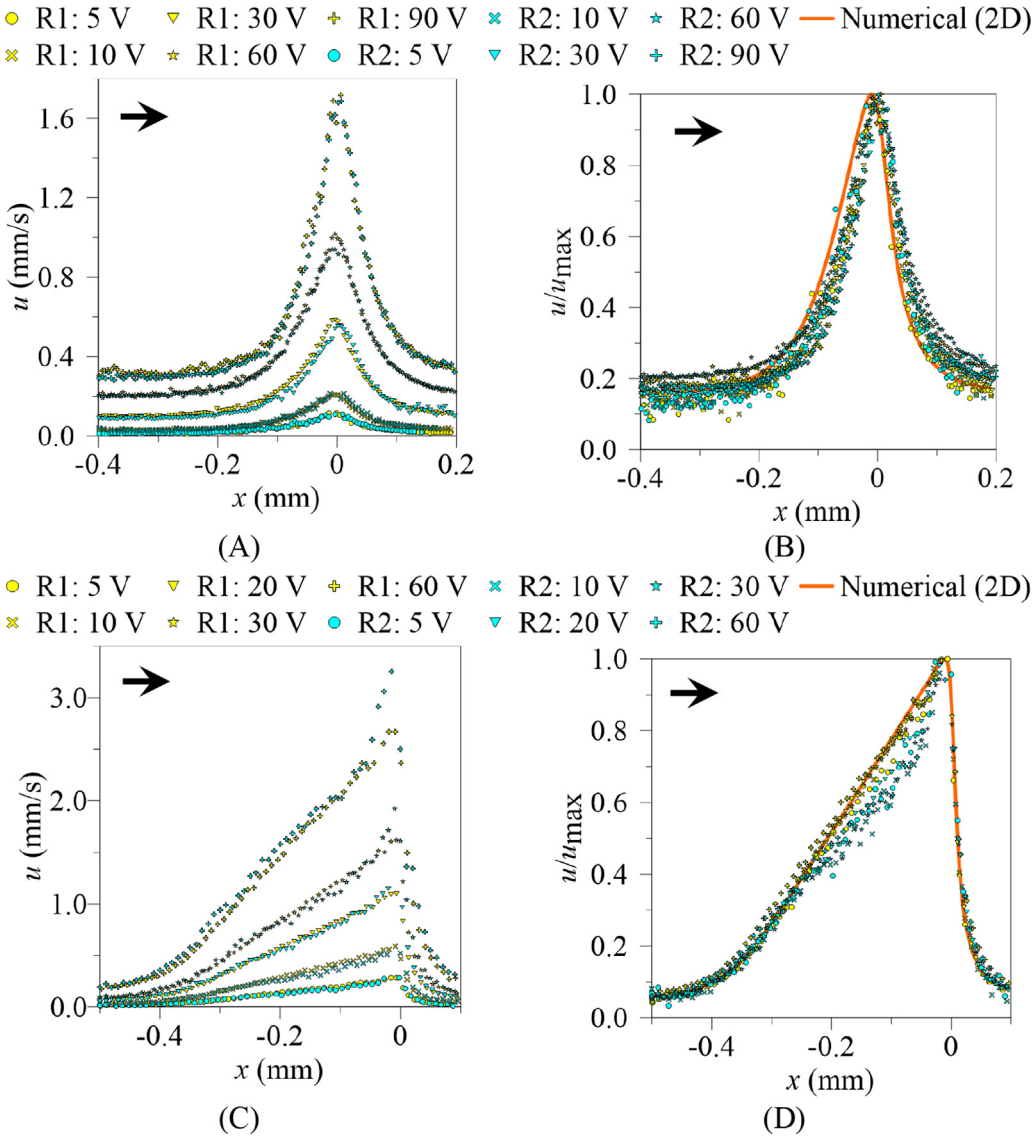

Fig. 4. Centerline velocity profiles measured at $z/H = 0.15$, in microchannels H_2−f (A) and H_3−f (C) for ΔV=5, 10, 30, 60 and 90V and ΔV=5, 10, 20, 30 and 60V, respectively using the 1 mM borate buffer with dye. Plots (B) and (D) each represent a comparison between the corresponding normalized velocity profiles with the velocity profile computed numerically for 2D flow, in microchannels H_2-f and H_3-f, respectively. Reynolds number at the throat is respectively 0.13 (90 V) and 0.084 (60 V) in microchannels H_2−f and H_3−f. The black arrows indicate the flow direction. R1 and R2 identify two different experimental runs, carried out exactly under the same conditions.

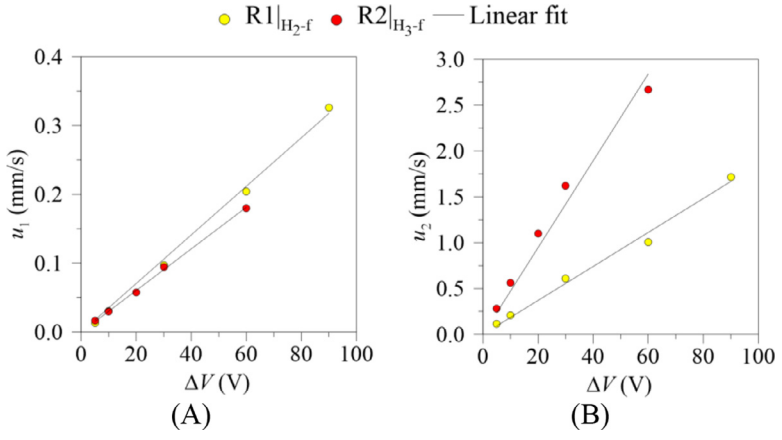

Fig. 5. Variation with imposed potential difference of the velocity (u_1) at the upstream channel (A) and maximum velocity (u_2) at the throat of the contraction (B) in microchannels H_2−f (R1), and H_3−f (R2), using the 1 mM borate buffer with dye.

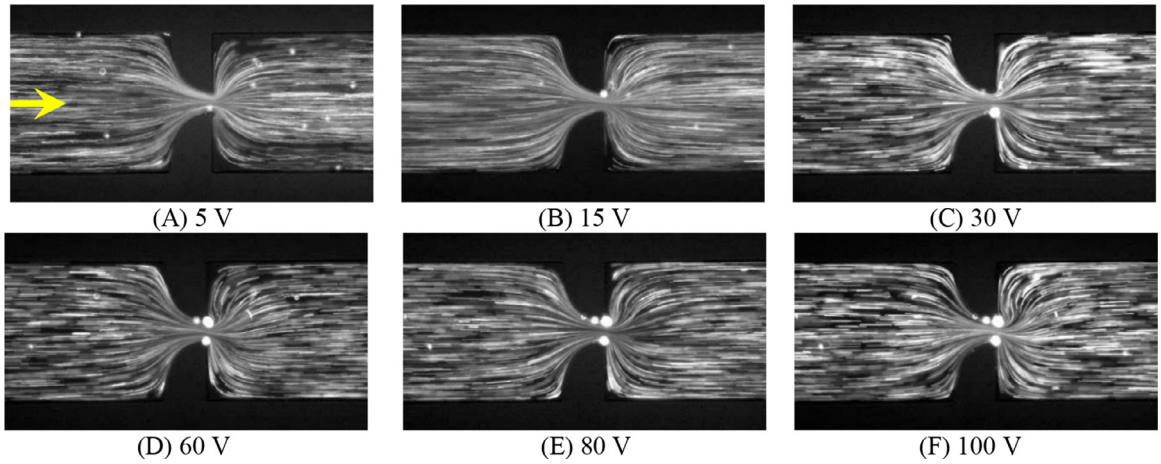

Fig. 6. Flow visualizations in microchannel H_2-f, using the 1000 ppm PAA solution: ΔV=5V (A), 15V (B), 30V (C), 60V (D), 80V (E), and 100V (F). The arrow indicates the flow direction.

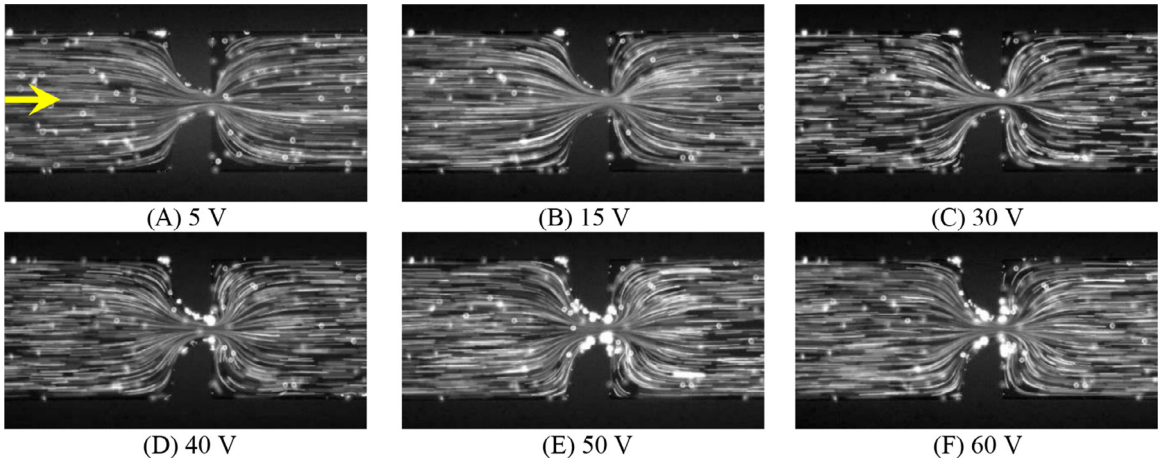

Fig. 7. Flow visualizations in microchannel H_2-f, using the 10000 ppm PAA solution: ΔV=5V (A), 15V (B), 30V (C), 40V (D), 50V (E), and 60V (F). The arrow indicates the flow direction.

Newtonian fluids a linear increase in the velocities with the imposed voltage (ΔV) is observed, as shown in Fig. 5.

3.3. Non-Newtonian fluids

The previous section presented the results for the Newtonian fluid and in all tested cases the flow was stable and symmetric relative to the y=0 plane. This section focus on the viscoelastic fluids, for which flow instabilities were found and are investigated for a range of flow conditions, including: geometry (H_2 and H_3), polymer concentration (100, 300, 1000, and 10000 ppm), imposed ΔV typically in the range between 2.5 and 140V, both in the forward and backward flow configurations. The imposed ΔV was increased slowly and gradually.

3.3.1. Microchannels H_2-f

Using the same flow settings as for Newtonian fluids described in Section 3.2.1, for polymer concentrations of 1000 and 10000 ppm, the corresponding flow visualizations for the forward flow are shown in Figs. 6 and 7, respectively. For the 1000 ppm solution, at low ΔV, the flow is Newtonian-like, with smooth and steady streamlines. Increasing ΔV to 60, 80 and 100V results in particle accumulation at the throat and these lead to the formation of a small vortex with bright spots immediately downstream of the throat, at the sudden expansion, cf. Figs. 6-(D) to (F). The accumulation of tracer particles at the throat should be avoided, because it leads to blocking effects and fictitious instabilities at the contraction, in particular at high imposed potential differences. Cleaning the channel between consecutive runs, reduces the accumulation of particles at the throat and eliminates some observed flow instabilities. Similarly, Fig. 7 presents the flow fields with the 10000 ppm solution. For ΔV<30V, the overall flow behavior is Newtonian-like, but as the imposed voltage progressively increases above 30V, flow streamlines deviate from the symmetry typical of the Newtonian-like flow field, especially on the downstream expansion even though in these cases the deviation is small, hence we consider the flow as quasi-steady, especially in the throat region. This deviation is most probably due to particle accumulation, rather than because of elastic effects even if these become stronger with flow rate.

Here, it is instructive to obtain a better and clear understanding of the flow behavior through the use of the PTV technique. The measurements were done at the mid-plane, z/H=0.5, of microchannel H_2-f, and the camera frame rate was set at 500 fps. Fig. 8 shows the pathlines (A, B, C) and centerline velocity profiles (D) for the 1000 ppm PAA solution, with Fig. 8-(E) representing the corresponding dimensionless velocity profiles obtained from Fig. 8-(D). Accordingly, by comparing the results presented in Figs. 8-(A) to (C) with the flow visualizations shown in Fig. 6, it is clear that identical pathlines are obtained using both techniques, while by comparing the dimensionless velocity profiles in Fig. 8-(E) with the experimental and 2D numerical Newtonian profiles, we find quantitatively different velocity profiles, suggesting that viscoelastic effects are important. In Fig. 8-(D), the Weissenberg and

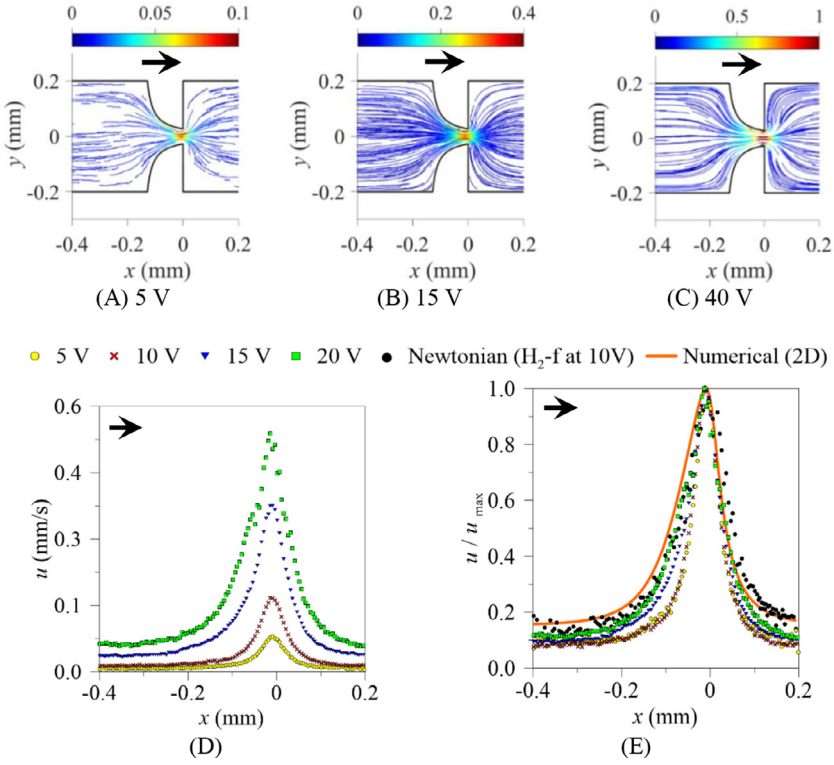

Fig. 8. Pathlines (A, B and C) and centerline velocity profiles (D) at $z/H = 0.5$ obtained using the PTV technique, in microchannel H_2-f, using the 1000 ppm PAA solution, for ΔV between 5 and 40V. Plot (E) shows the corresponding dimensionless velocity profiles of plot (D). The color bar represents the velocity magnitude in mm/s, while the black arrows indicate the flow direction.

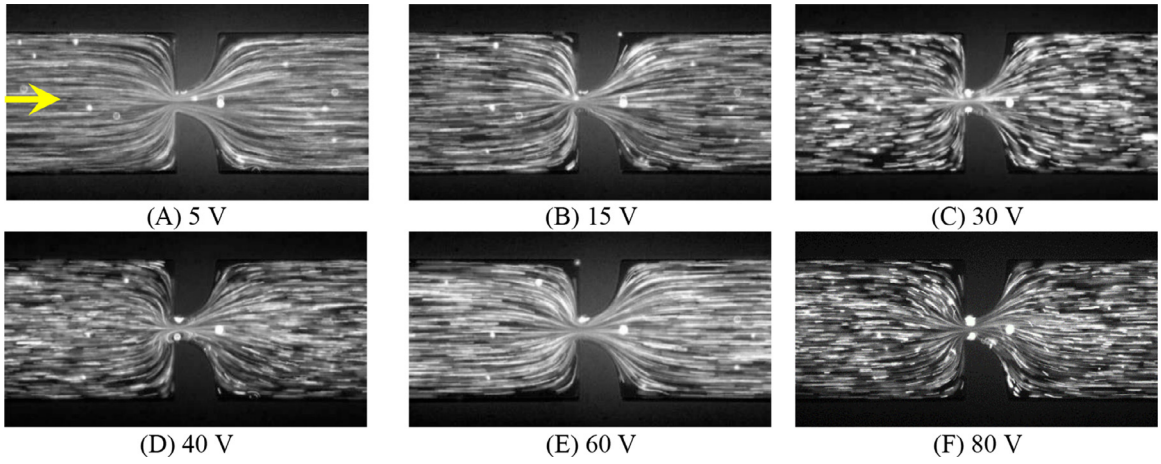

Fig. 9. Flow visualizations in microchannel H_2-b, using the 1000 ppm PAA solution: ΔV=5V (A), 15V (B), 30V (C), 40V (D), 60V (E), and 80V (F). The arrow indicates the flow direction.

Reynolds numbers for ΔV varying between 5 and 20V vary between 9.61×10^{-4} and 6.36×10^{-3}, and 3.15×10^{-3} and 2.14×10^{-2}, respectively. We note that the estimated *Wi* values are low because they are based on bulk flow characteristics. If instead the Debye layer thickness was used as characteristic length scale much higher *Wi* would occur.

3.3.2. *Microchannels H_2-b*

By inverting the electrode polarity, the flows are reversed occurring now through abrupt contractions and hyperbolic expansions. Figs. 9 and 10 show the corresponding observed tracer particle pathlines for the same PAA concentrations of 1000 and 10000 ppm, respectively. Now, the flows show a more complex flow behavior for ΔV above 15 to 30V for the 1000 ppm solution and ΔV above 5 to 15V for the 10000 ppm solution, with the noticeable formation of regions of unstable flow at each corner of the throat, where tracer particles recirculate. For the 1000 ppm solution the instabilities become clear from 30 to 80V, as shown in Figs. 9-(C) to (F), whereas for the 10000 ppm solution the upstream flow instabilities become even more clear and grow significantly while increasing the imposed electric potential from $\Delta V = 10$ to 20V, see Fig. 10-(C) and (D). For $\Delta V = 20$ to 30V the flow becomes more unstable, see Fig. 10-(D) and (F). Similarly, on the downstream expansion the unstable flow progresses from having low intensity recirculations at $5V < \Delta V < 15V$ to high instability recirculations for $\Delta V > 15V$.

The 1000 ppm solution is a Boger-like fluid, i.e., a viscoelastic fluid of nearly constant shear viscosity, and these instabilities have not been observed in the corresponding Newtonian flows, therefore we attribute them to fluid elasticity. By increasing the polymer concentration, elastic effects become more pronounced and even though the viscosity is no longer independent of the shear rate, the shear-thinning level is still not intense and fluid elasticity predominates. Further increasing the imposed potential difference, flow instabilities grow and extend gradually

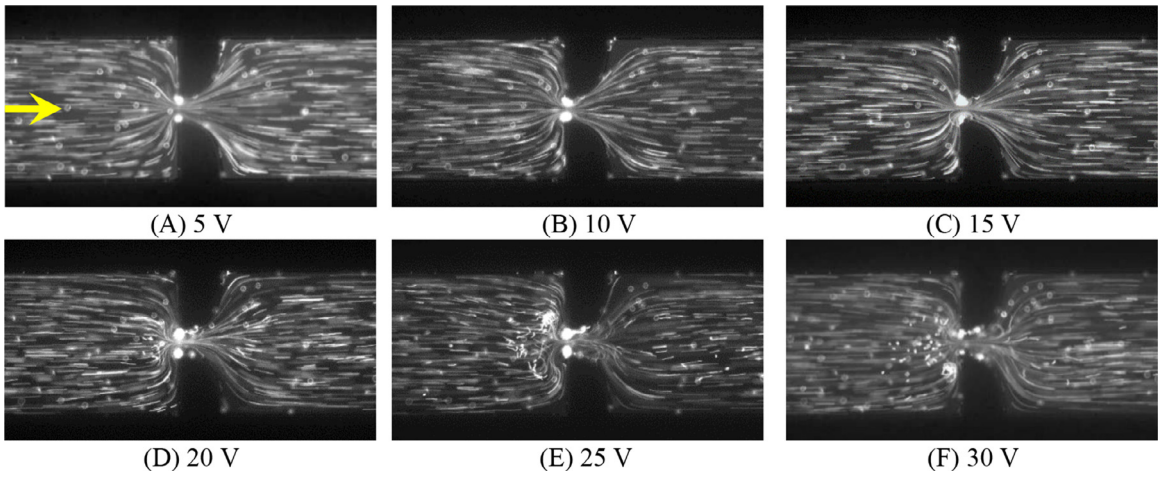

Fig. 10. Flow visualizations in microchannel H_2-b, using the 10000 ppm PAA solution: ΔV=5V (A), 10V (B), 15V (C), 20V (D), 25V (E), and 30V (F). The arrow indicates the flow direction.

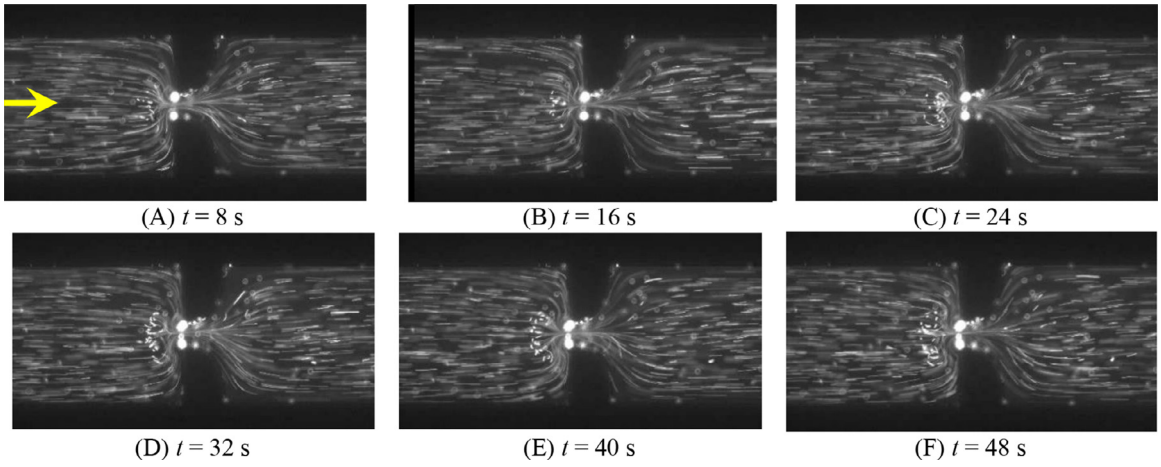

Fig. 11. Evolution with time of flow behavior for an imposed ΔV = 25 V in microchannel H_2-b, using the 10000 ppm PAA solution. The arrow indicates the flow direction.

to influence the whole flow field both upstream and downstream of the throat. The elastic effects are seen to be more significant in the backward configuration, because the sudden contraction imposes a more abrupt restriction than the hyperbolic contraction, and this can lead to more intense flow variations as was found by Matos et al. [30] for surfactant solutions.

The flow instability shown in Fig. 10-(E) is illustrated in more detail in Fig. 11, pertaining to a single run and showing in its various parts the time evolution of the flow patterns. A low intensity instability is observed close to the throat region, characterized by a quasi-steady symmetric (relative to y=0), vortex.

Similarly, by using the same setting as in Fig. 8, and by comparing the pathlines of Figs. 12-(A) to (C) with Fig. 9, it is easier now to observe small recirculation zones at the throat corner for the backward flow direction. These separated flow regions exist both upstream and downstream of the contraction plane. They are clearly different from the separated flow regions observed in pressure driven flow of viscoelastic polymer solutions through contractions, where the symmetric vortices are located and developed at the upstream of the contraction [18]. Additionally, Fig. 12-(D) and (E) shows that for ΔV> 5 to 20V, there is a significant change in the velocity field near the minimum throat cross sectional area followed by a smoother decrease of the velocity profile downstream of the throat. The Weissenberg and Reynolds numbers for ΔV between 5 and 20V vary between 7.25×10^{-4} and 3.82×10^{-3}, and 2.65×10^{-3} and 1.31×10^{-2}, respectively.

In summary, for microchannel H_2, stable Newtonian-like flows are observed in the upstream channel for the 1000 and 10000 ppm PAA fluids in the forward direction, whereas in the backward flow direction a recirculating zone is formed at each corner of the throat leading to some instability. Increasing the polymer concentration to 10000 ppm, leads to an instability downstream the throat in the forward configuration, and more intensively in the backward configuration. All instabilities are further enhanced at higher electric potential differences. Even though these instabilities appear to be stronger in the backward flow configuration, the forward flow is not devoid of instabilities, showing deviations from the Newtonian-like behavior at the highest ΔV tested for the more concentrated polymer solution.

3.3.3. *Microchannels H_3-f*

The flow patterns observed in the higher Hencky strain microchannel (H_3-f) are shown in Figs. 13 and 14 for PAA solutions at concentrations of 300 and 1000 ppm, respectively. Instabilities are seen to take place even when the polymer concentration is low (300 ppm). At each concentration, the flow is Newtonian-like below a critical potential difference (around ΔV=5V for 300 ppm PAA concentration) whereas at higher ΔV, elastic-driven instabilities start to develop upstream of the throat in the converging region, see Fig. 13-(B). This flow is now characterized by a pair of steady symmetric upstream vortices that increase in strength with the imposed potential difference, see Fig. 13-(B) to (G). This is akin to some elastic behavior observed in pressure-driven flow of

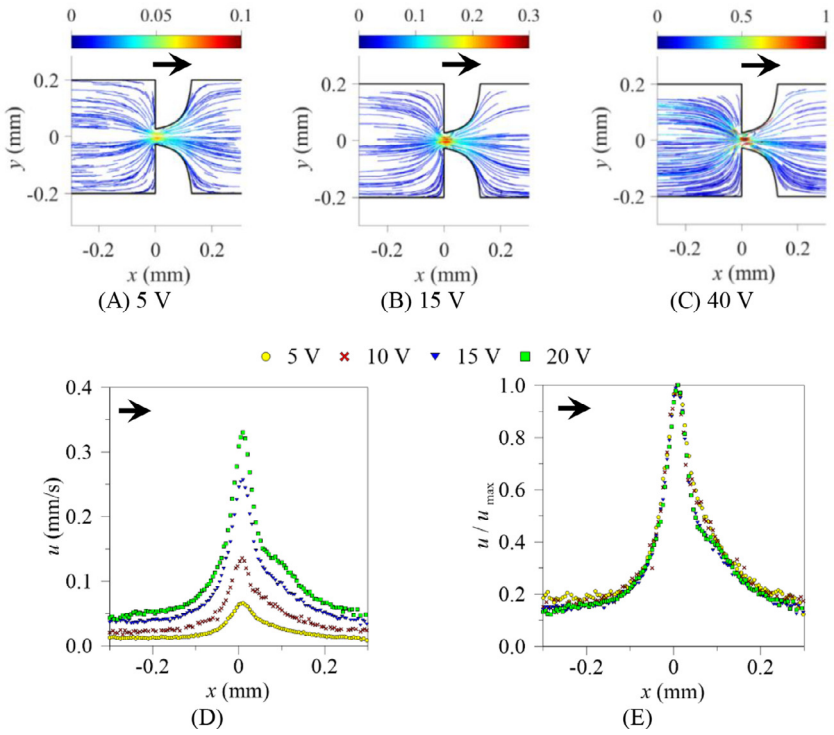

Fig. 12. Pathlines (A, B and C) and centerline velocity profiles (D) at $z/H = 0.5$ obtained with the PTV technique, in microchannel H_2-b, using the 1000 ppm PAA solution, for ΔV between 5 and 40V. Plot (E) shows the corresponding dimensionless velocity profiles of plot (D). The color bar in A-C represents the velocity magnitude in mm/s, while the black arrows indicate the flow direction.

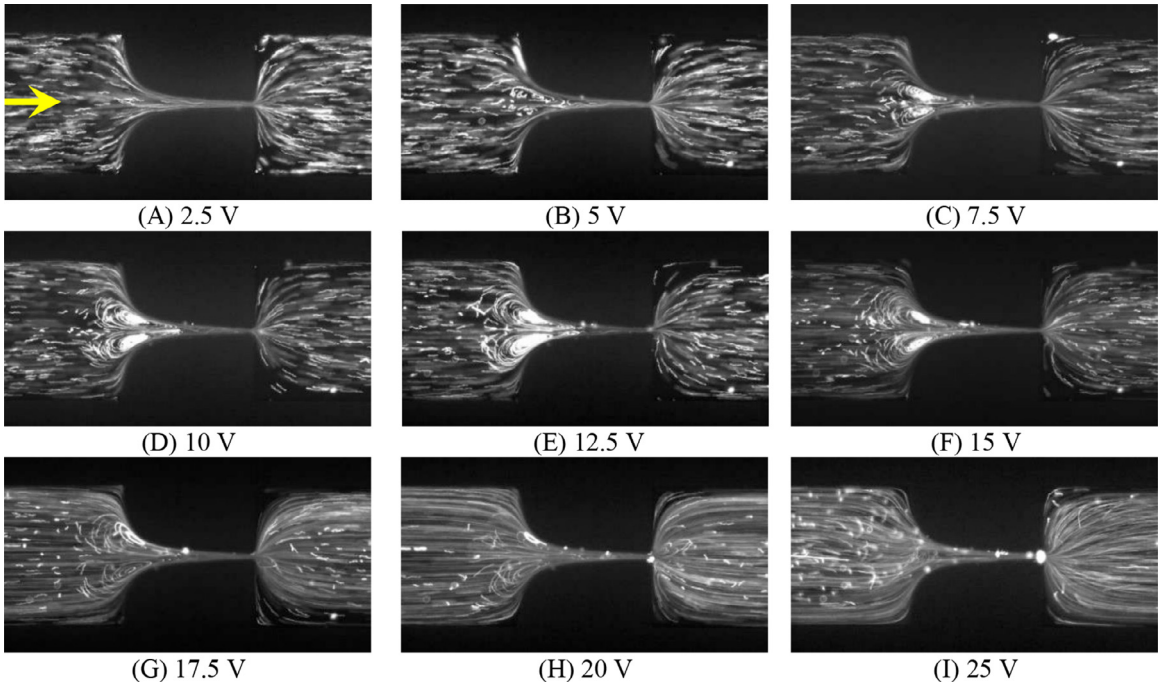

Fig. 13. Flow visualizations in microchannel H_3-f, using the 300 ppm PAA solution: ΔV=2.5V (A), 5V (B), 7.5V (C), 10V (D), 12.5V (E), 15V (F), 17.5V (G), 20V (H), and 25V (I). The arrow indicates the flow direction.

viscoelastic fluids at low *Re* [18,19,26]. Further increasing the potential difference, the recirculating flow becomes stronger, but remains steady, as shown in Fig. 13-(G) to (I). However, over time it may become also chaotic-like at high ΔV because of particle accumulation at the throat. A similar behavior is observed for the 1000 ppm polymer solution but, due to its higher elasticity, the characteristic elastic flow patterns appear at lower ΔV and are more intense than those seen with the 300 ppm polymer solution, see Fig. 14-(A) to (I). Also, the accumulation with time of tracer particles at the throat leads to unsteady flow at a lower ΔV than with the 300 ppm solution, under the same circumstances. Since these instances of unsteady flow are due to particle accumulation, they will not be reflected on the map of flow regimes presented later in Section 3.3.5.

To better understand the flow behavior, Fig. 14-(D) includes an interpretative sketch of the flow direction within the separated flow regions (colored in red) corresponding to a steady symmetric flow. A large sep-

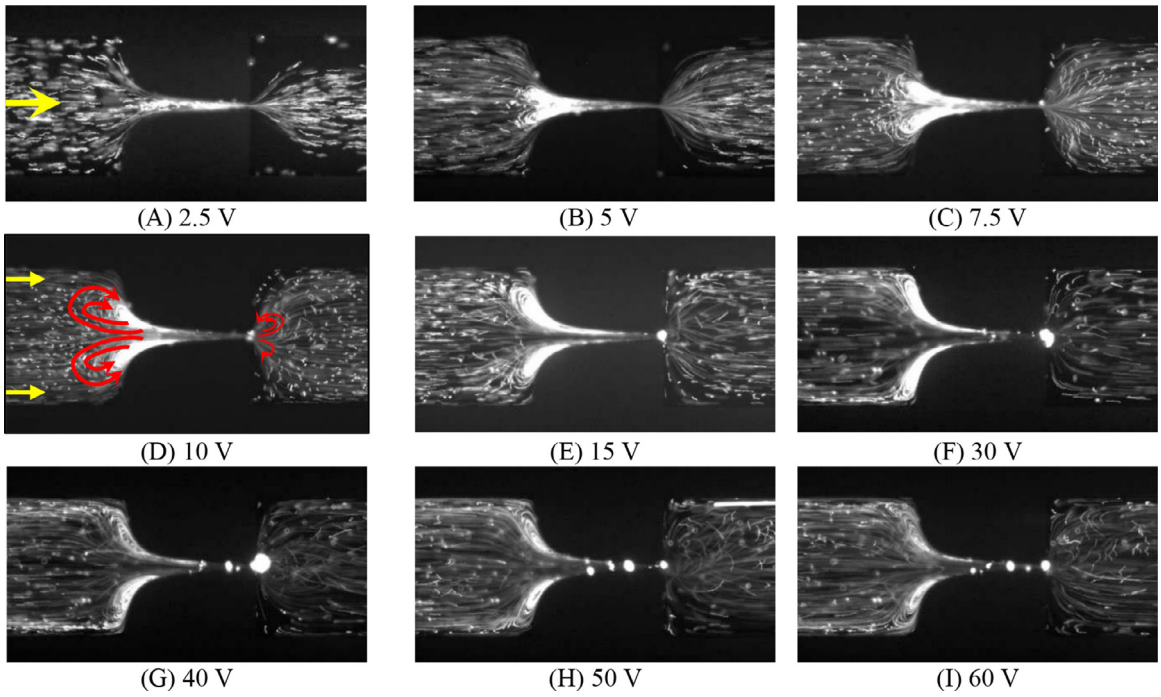

Fig. 14. Flow visualizations in microchannel H_3-f, using the 1000 ppm PAA solution: ΔV=2.5V (A), 5V (B), 7.5V (C), 10V (D), 15V (E), 30V (F), 40V (G), 50V (H), and 60V (I). The yellow arrow indicates the flow direction. The red lines at (D) sketch the flow direction within the steady symmetric flow regions. (For interpretation of the references to color in this figure legend, the reader is referred to the web version of this article.)

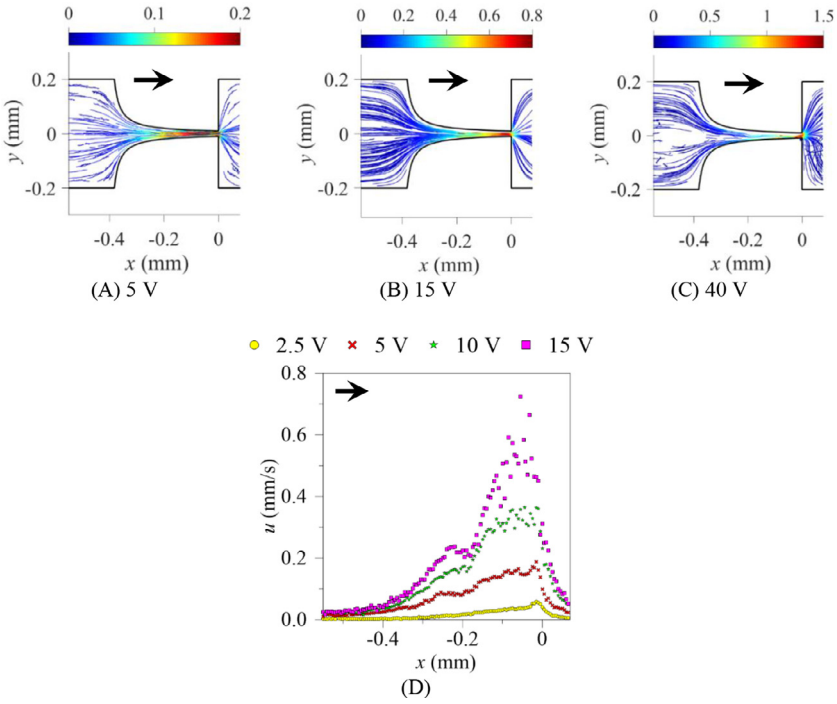

Fig. 15. Pathlines (A, B and C) and centerline velocity profiles (D) at z/H = 0.5 obtained using the PTV technique, in microchannel H_3-f, using the 300 ppm PAA solution, for ΔV between 2.5 and 40V. The color bar in A-C represents the velocity magnitude in mm/s, while the black arrows indicate the flow direction.

arated flow region is observed upstream of the throat, and a small one is also seen downstream of the throat.

Similarly using the same setting of Fig. 8, the flow patterns as well as the centerline velocity profiles are explored for microchannel H_3-f with the 300 ppm solution, as shown in Figs. 15-(A) to (C), and Fig. 15-(D), respectively. It is clear from Figs. 15-(A) to (C), that the PTV technique faces some difficulties to track well the pathlines in the upstream recirculation. This suggests a limitation due to the limited number of tracer particles (TPs) within the recirculation region and due to the velocity difference between TPs within and outside the recirculation, or also because the unstable flow is more complex, with a more intense velocity component normal to the plane of measurement, and TPs could become out of focus easily. For the centerline velocity in Fig. 15-(D), the observed profile at ΔV=2.5V slightly differs from the Newtonian fluid

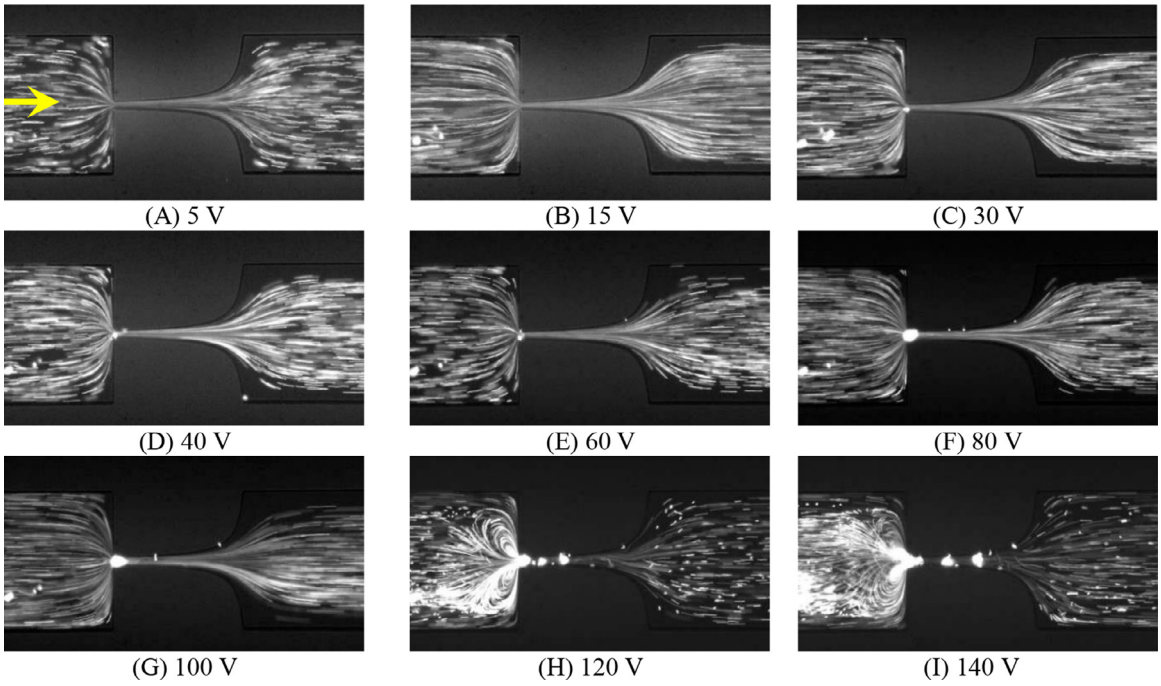

Fig. 16. Flow visualizations in microchannel H_3-b, using the 100 ppm PAA solution: ΔV=5V (A), 15V (B), 30V (C), 40V (D), 60V (E), 80V (F), 100V (G), 120V (H), and 140V (I). The arrow indicates the flow direction.

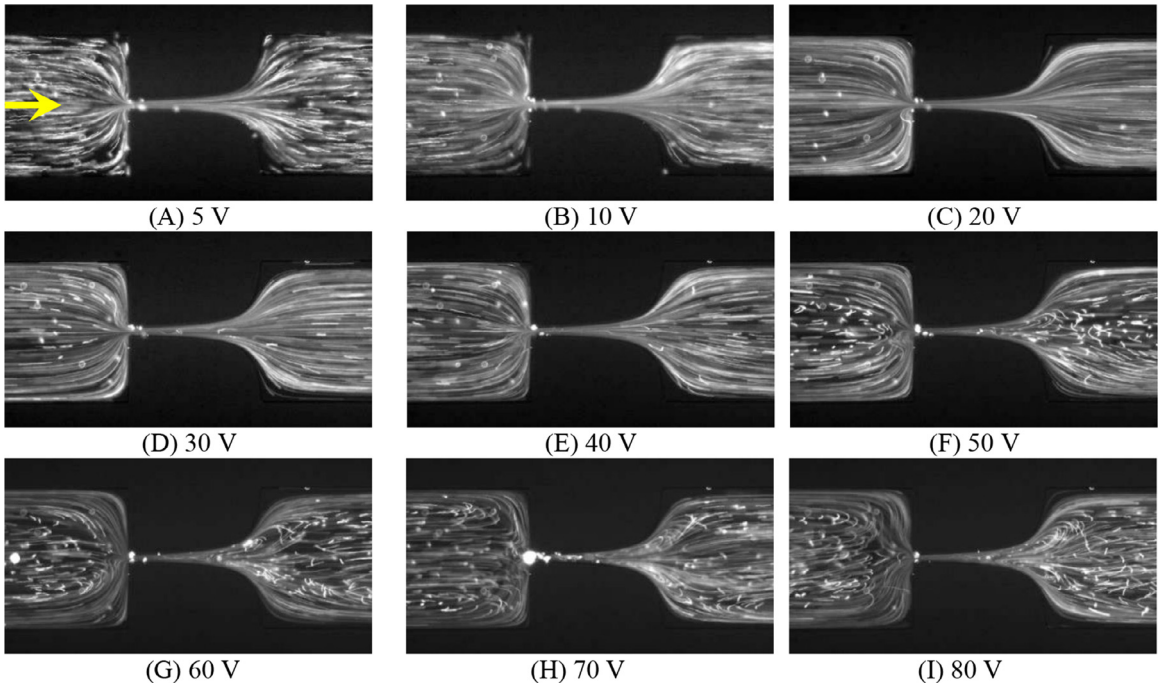

Fig. 17. Flow visualizations in microchannel H_3-b, using the 300 ppm PAA solution: ΔV=5V (A), 10V (B), 20V (C), 30V (D), 40V (E), 50V (F), 60V (G), 70V (H), and 80V (I). The arrow indicates the flow direction.

profiles (cf. Fig. 4-(C)), where a small peak in the velocity is observed at the throat which should be the outcome of elasticity. Additionally, at $\Delta V \geq 5$V, the velocity profiles are not increasing linearly in the hyperbolic upstream contraction, due to the formation of upstream vortices changing the shape of the contracting flow as previously shown in Figs. 13-(B), (D), and (F). In Fig. 15-(D), the Weissenberg and Reynolds numbers for ΔV between 2.5 and 15V vary between 8.72×10^{-5} and 1.08×10^{-3}, and 1.52×10^{-3} and 1.86×10^{-2}, respectively.

3.3.4. *Microchannels H_3-b*

The flow behavior observed with microchannel H_3-b is shown in Figs. 16, 17 and 18 for the 100, 300, and 1000 ppm PAA concentrations, respectively. In these plots the images are mirrored, so that the flow is from left to right. Again, a gradual elasticity-driven flow pattern progressively evolves from a Newtonian-like flow as ΔV increases. There is a potential difference for which we clearly observe the development of such elastic flow features as regions of separated

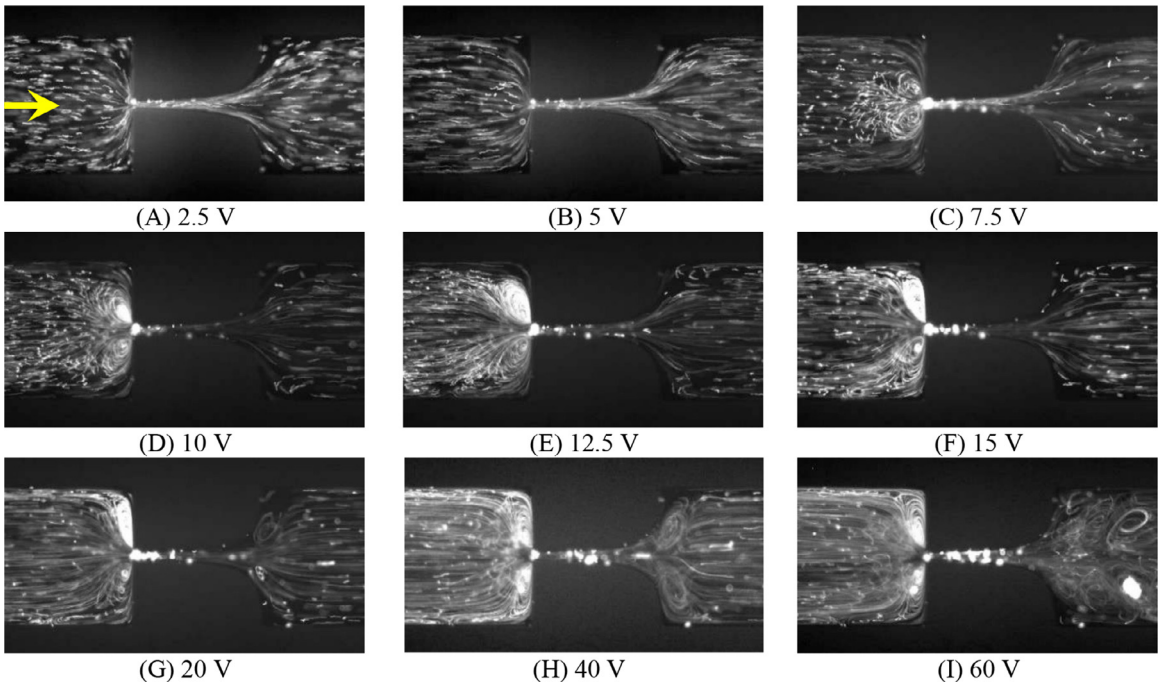

Fig. 18. Flow visualizations in microchannel H_3-b, using the 1000 ppm PAA solution: ΔV=2.5V (A), 5V (B), 7.5V (C), 10V (D), 12.5V (E), 15V (F), 20V (G), 40V (H), and 60V (I). The arrow indicates the flow direction.

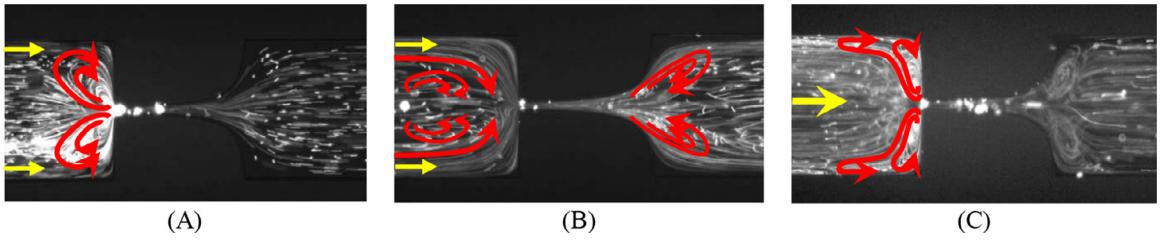

Fig. 19. Schematic representation of flow features (in red), showing the flow direction within the separated flow regions, in microchannel H_3-b using (A) 100 ppm PAA solution, for ΔV=120V, (B) 300 ppm PAA solution, at ΔV=60V, and (C) 1000 ppm PAA solution, with ΔV=40V. The yellow arrows indicate the flow direction. (For interpretation of the references to color in this figure legend, the reader is referred to the web version of this article.)

flow, which decreases with the increase of polymer concentration: around 80V for the 100 ppm solution (see Figs. 16-(F) to (I)), 50V for the 300 ppm solution (see Fig. 17-(F) to (I)), and 2.5V for the 1000 ppm solution (see Fig. 18-(A)-(I)). For the 1000 ppm solution, a time-dependent instability is observed on the throat downstream side, provided that $\Delta V \geq$ 20V (Fig. 18-(G) to (I)), while a quasi-steady symmetric flow remains on the throat upstream side. Increasing ΔV leads to higher flow rates and more intense elastic-driven instabilities upstream of the contraction throat, which then propagate downstream at higher ΔV.

Fig. 19-(A) to (C) illustrates the flow pattern within the separated flow region, corresponding to the flow case shown in Figs. 16-(H), 17-(G), and 18-(H), respectively. As shown in Fig. 19-(A), whereas upstream the flow is already unstable, but still steady, downstream of the throat the flow behavior is still Newtonian-like. Increasing the polymer concentration, as shown in Fig. 19-(B), regions of separated flow are observed upstream and downstream of the throat, where the flow is characterized by quasi-steady and symmetric flow features, especially if $\Delta V \geq$ 50V. Further increasing the concentration to 1000 ppm as, in Fig. 19-(C), the flow is now characterized by two steady symmetric separated flow regions upstream of the throat, followed by two time-dependent separated flow regions downstream of the throat.

The time evolution of the flow field from the rest state is illustrated in Figs. 20 and 21 for conditions corresponding to a final established unstable flow. Fig. 20 considers the flow of a 300 ppm PAA solution with ΔV=60V, whereas Fig. 21 pertains to the 1000 ppm solution at ΔV=40V. In Fig. 20, there are regions of separated flow forming both upstream and downstream of the throat, both exhibiting a quasi-steady symmetric behavior. Additionally, it was realized that once tracer particles accumulate at the throat, it owes much to downstream recirculation where the backward flow feeds the throat region with tracer particles, as shown in Fig. 20-(D) to (F). For the 1000 ppm solution in Fig. 21, a strong instability is observed with the onset of a time-dependent instability and a quasi-steady symmetric flow on the throat downstream and upstream sides, respectively. These features can be seen in the series of pictures of Fig. 21, all pertaining to different times at ΔV=40V. By observing this flow field evolution over time (Fig. 21-(A) to (F)), it is clear that downstream of the throat, the flow shows a cyclic behavior of instability, with the vortices being formed and then collapsing over time. It is also observed that over time tracer particles accumulate and stick to the microchannel walls, which influences the observed instability, but this is not the cause of the instability because initially there were no accumulated particles. Upstream of the throat, the flow is more stable.

Using similar settings as in Fig. 8, the results shown in Fig. 22 for microchannel H_3-b with the 300 ppm PAA solution suggest the same con-

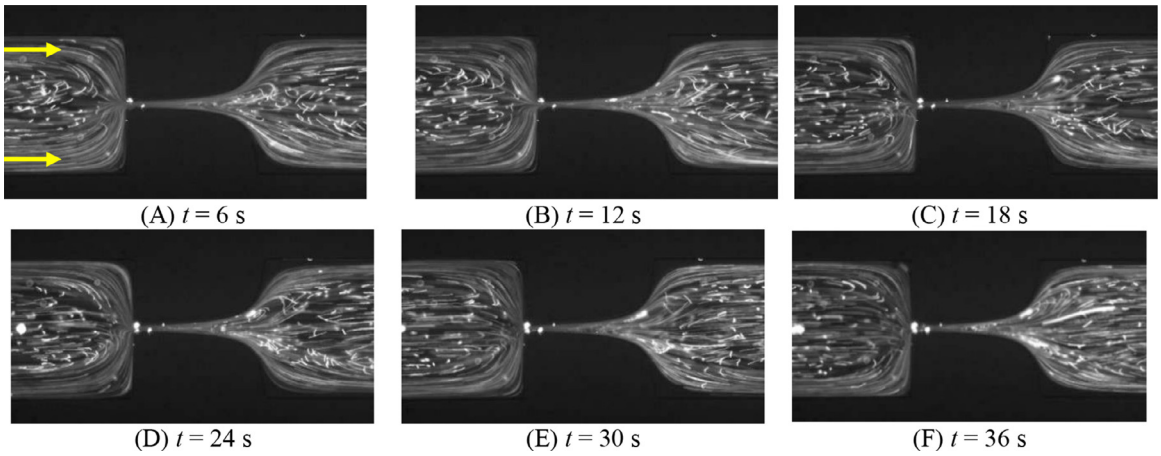

Fig. 20. Evolution with time of flow behavior for ΔV=60V in microchannel H_3-b, using the 300 ppm PAA solution. The arrows indicate the flow direction.

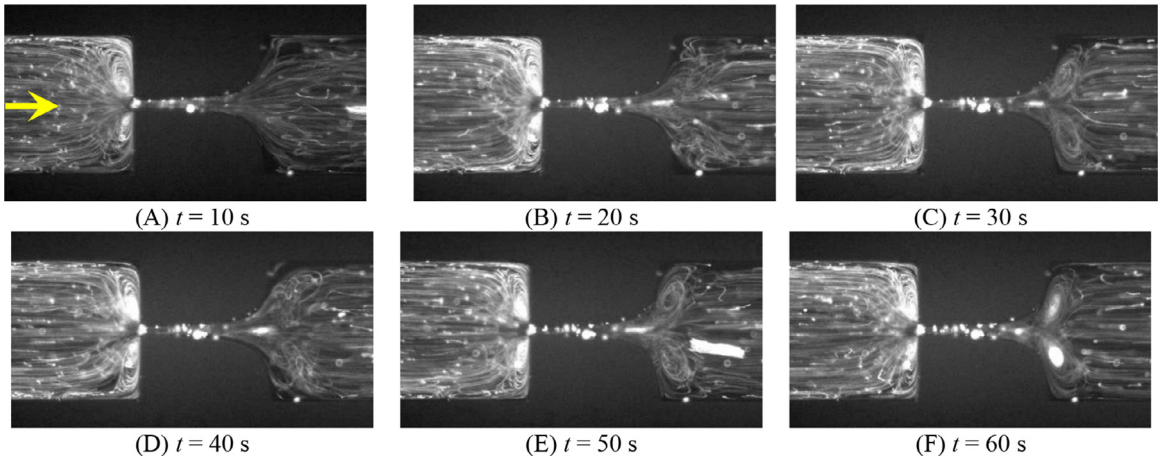

Fig. 21. Evolution with time of flow behavior for ΔV=40V in microchannel H_3-b, using the 1000 ppm PAA solution. The arrow indicates the flow direction.

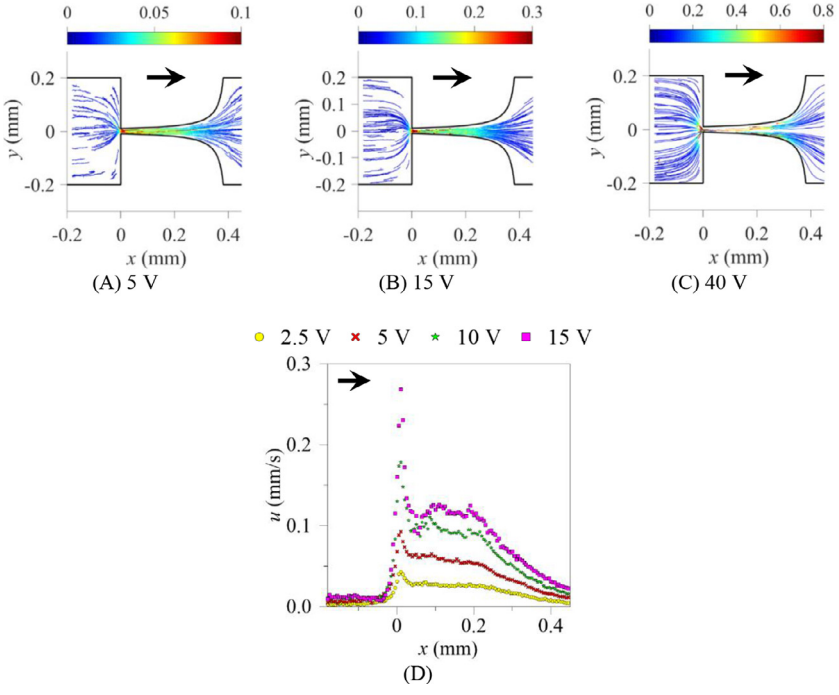

Fig. 22. Pathlines (A, B and C) and centerline velocity profiles (D) at z/H = 0.5 obtained using the PTV technique, in microchannel H_3-b, using the 300 ppm PAA solution, for ΔV between 2.5 and 40V. The color bar represents the velocity magnitude in mm/s, while the black arrows indicate the flow direction.

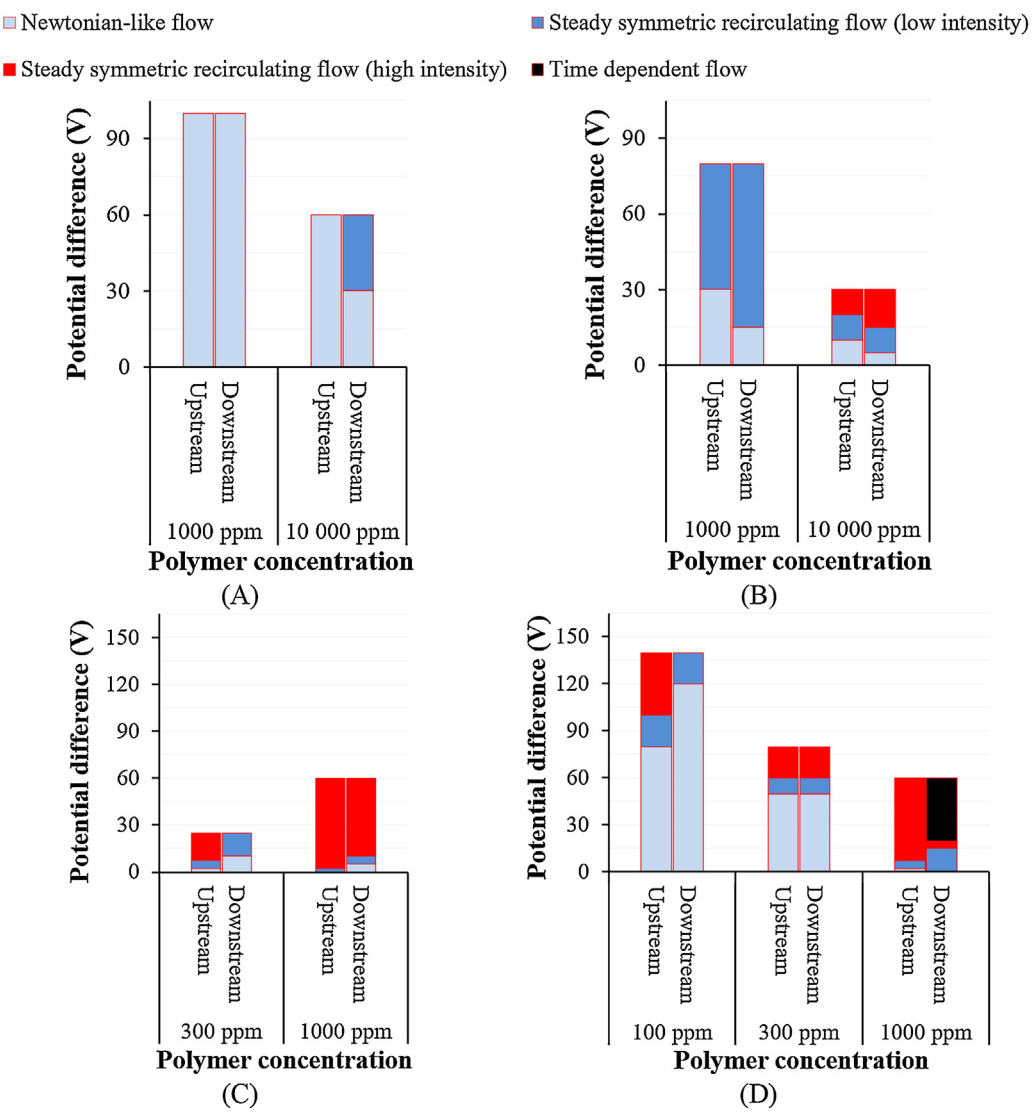

Fig. 23. Flow chart in terms of electrical potential-polymer concentration parameters representing the type of flow in microchannels H_2-f (A), H_2-b (B), H_3-f (C), and H_3-b (D).

clusions reached for Fig. 15-(A) to (C), regarding the difficulties faced by PTV to identify the recirculating flow patterns of tracer particles upstream and downstream of the throat, see Fig. 22-(A) to (C). Fig. 22-(D), at ΔV=2.5V, suggests a stronger elastic effect in the backward flow, where a larger velocity peak is observed at the throat in comparison with Fig. 15-(D) for the same ΔV=2.5V. Such type of velocity overshoots are typically observed in abrupt contraction flows of viscoelastic fluids [31]. This velocity peak is followed by a complex non-monotonic decrease in velocity along the hyperbolic expansion, which can reflect the occurrence of a flow instability at the throat and its downstream region. In Fig. 22-(D), the Weissenberg and Reynolds numbers vary between 6.47×10^{-5} and 3.94×10^{-4}, and 1.17×10^{-3} and 6.89×10^{-3}, respectively, for ΔV between 2.5 and 15V.

In summary, for microchannel H_3-f, steady flow fields, differing significantly from the Newtonian-like flow, are seen for PAA solutions with concentrations of 300 and 1000 ppm, whereas in the backward flow direction a time-dependent flow behavior is observed with the 1000 ppm solution, here characterized by a quasi-steady instability upstream of the throat and a time-dependent flow instability downstream of the throat. In conclusion, microchannel H_3 leads to enhanced flow instabilities in comparison with microchannel H_2, primarily due to the higher Hencky strain.

3.3.5. *Flow mapping for microchannels H_2 and H_3*

As can be concluded from the previous sections, depending on the polymer concentration, imposed electric potential difference, and microchannel configurations (i.e. H_2-f, H_2-b, H_3-f, or H_3-b), different flow characteristics are observed, spanning from a quasi-Newtonian flow pattern at the upstream and downstream regions at low ΔV, up to electroelastic flow instabilities above a critical imposed electric potential. As discussed, the accumulation of particles at the throat further destabilizes the flow, but these effects can be minimized through the use of clean microchannels. The map of Fig. 23 was drawn under these clean conditions. The velocity profiles presented in Sections 3.3.1 to 3.3.4 facilitate the determination of either the maximum Weissenberg number that can be reached without occurrence of flow instabilities, or the critical Weissenberg number (Wi_{cr}) above which flow instabilities may occur (again, cases where particles clog at the throat were not considered). The transition from Newtonian-like flow to one of the unstable flow conditions is usually characterized by the presence of steady flow separation. We note that the low Wi values reported in the previous sections are based on bulk quantities, but the local Weissenberg number evaluated based on the shear rate at the Debye layer could be significantly higher, as discussed by Pimenta and Alves [21]. Due to the lack of information, it is very difficult to estimate realistic values of the Debye layer thickness

in these experiments, and for water or water- based fluids it is known from the literature that the Debye layer widths can vary by more than two orders of magnitude [32].

In conclusion, to summarize all of the experiments that were carried out using viscoelastic aqueous solutions of PAA at several concentrations, Fig. 23 presents a flow chart to illustrate the different flow types observed in the electrical potential-polymer concentration parameter space, pertaining to microchannels H_2 and H_3, both in the forward and backward flow directions, considering both the flow at the microchannel upstream and downstream regions. It is clear from Fig. 23-(D) that it is for the higher Hencky strain geometry in the backward flow direction (H_3-b, ϵ_H=3) that a richer flow dynamics is observed, especially for the highest polymer concentration (1000 ppm). As the imposed potential difference is increased the following sequence of flow patterns is observed: Newtonian-like flow; steady symmetric recirculating flow of low intensity; steady symmetric recirculating flow of high intensity; time dependent flow. As mentioned before, this map does not consider further flow instabilities associated with the deposition and accumulation of tracer particles at the throat over time. This is a particular problem in geometries with long throats, as is the case of both H3 contraction-expansions.

4. Concluding remarks

This work presented EOF of Newtonian and viscoelastic fluids in different abrupt and hyperbolic contraction/expansions. The Newtonian fluid was used to understand the flow behavior in the linear regime for each of the microchannels. Using a Newtonian aqueous solution of 1mM borate buffer, the following conclusions were obtained: in the tested range of imposed electric fields, dielectrophoresis has negligible effect on the tracer particles pathlines, a quasi-uniform extension rate is observed along the centerline of the hyperbolic contraction, and the flow behavior remains stable, even at the highest ΔV tested.

On the less positive side, two main problems were faced. On one hand, poor image quality was typically observed when measuring the centerline velocity profiles particularly at high ΔV, but this drawback was circumvented by adding a small amount of fluorescent dye to improve the image contrast, which helped in the image post-processing, allowing to operate the high-speed camera at higher frame rates. The second problem was due to particle accumulation at the walls, especially at the throat of the microchannels. This difficulty was minimized by removing the particles from the throat of the contraction between successive runs, by manually pressing gently the microchannel to apply some pressure gradient, but at high ΔV the tracer particles accumulation could not be avoided.

The viscoelastic effects on the flow field and flow stability were examined using viscoelastic aqueous solutions of PAA at concentrations between 100 and 10000 ppm. Two microchannels H_2 and H_3 were selected for the experiments, to analyze the instability conditions in both the forward (i.e. H_2-f and H_3-f) and backward (i.e. H_2-b and H_3-b) flow directions and the following conclusions were obtained:

- For microchannel H_2, a typically stable laminar flow behavior was observed in the forward flow direction, while a less stable flow was observed in the backward flow direction, which progressively leads to some instability by increasing polymer concentration.
- For microchannel H_3, which has a higher Hencky strain, typically steady flow behavior was observed with flow recirculation for almost all tested flows with polymer concentrations of 300 and 1000 ppm in the forward flow direction, while a typically time-dependent flow behavior was observed for the backward flow direction, especially downstream of the throat at higher polymer concentrations, thus leading to improved mixing.

In summary, for viscoelastic fluids and for each of the tested microchannels (H_2 or H_3), the forward flow direction was found to be more stable. Accordingly, microchannel H_2-f is more useful to investigate the flow behavior under homogenous strain rate for viscoelastic fluids, which can be particularly useful for rheology measurements [33,34], while microchannel H_3-b is better suited to promote fluid mixing, due to the strong electro-elastic instabilities that are generated at high electric fields. Nevertheless, in solutions containing tracer particles, there is a tendency for the particles to stick and accumulate at the throat walls over time, effectively changing the geometry shape and anticipating flow instabilities to lower electric potentials.

The experimental measurements of the polymer solutions in these channels were not easy to conduct, and many practical problems had to be overcome, such as tracer particle accumulation at the throat of the microchannels, and possible gel formation at high electric fields, among others. In practice, this work opens the way for detailed measurements of the velocity field within the microchannels that will allow, for instance, an adequate quantification of the Weissenberg number. Indeed, the values of *Wi* reported are very low, and yet the flows show instabilities of elastic origin, suggesting that a more adequate characteristic rate of deformation needs to be used, such as the shear rate at the Debye layer, but such quantity needs detailed velocity profile measurements. Also, the quantification of the critical Weissenberg numbers require a more refined set of measurements, around the critical conditions.

Declaration of Competing Interest

The authors declare no conflict of interest.

Acknowledgments

The authors acknowledge financial support from FCT (Fundação para a Ciência e a Tecnologia) through the PhD scholarship [SFRH/BD/85971/2012], and projects UIDB/00532/2020 and UIDP/00532/2020. The advice of Francisco Pimenta with the simulations and data processing is gratefully acknowledged.

Appendix A

To perform accurate PTV measurements of the centerline velocity with the 20X objective and the high-speed camera, it is necessary to carefully define the edges of the hyperbolic PDMS contraction walls. In addition, it is also necessary to ensure a sufficient number of detectable tracer particles (TPs) by appropriate selection of the light intensity considering the level of background noise and the light intensity from in-focus and out-of-focus TPs. In these experiments a Newtonian aqueous solution of 1 mM borate buffer seeded with 1.0 μm TPs was used, but dye was also added to the Newtonian fluid mainly to improve image quality. At high flow rates, it was found that adding a small amount of fluorescent dye made the light intensity from each individual in-focus TP to stay at similar level, especially in the throat region. This allowed the TPs to be fully tracked along the microchannel centerline. In contrast, not adding dye to the solution reduced the probability to fully track each individual in-focus TP along the centerline, especially in the throat region, where its velocity increases and the imaged light intensity decreases significantly.

To overcome these limitations, Fig. A.1 presents a series of snapshots for microchannel H_2−f with the Newtonian fluid and TPs at rest, at different depths, starting from the lower wall ($z = 0$) (Fig. A.1-(A)) up to the upper wall ($z = H$) (Fig. A.1-(I)). It is clear that at the depths in the range $0.15 \leq z/H \leq 0.85$, the edges of each wall are clearly defined and even the bright spot of each in-focus individual TP is clearly focused, in contrast to the region in the vicinity of the upper wall.

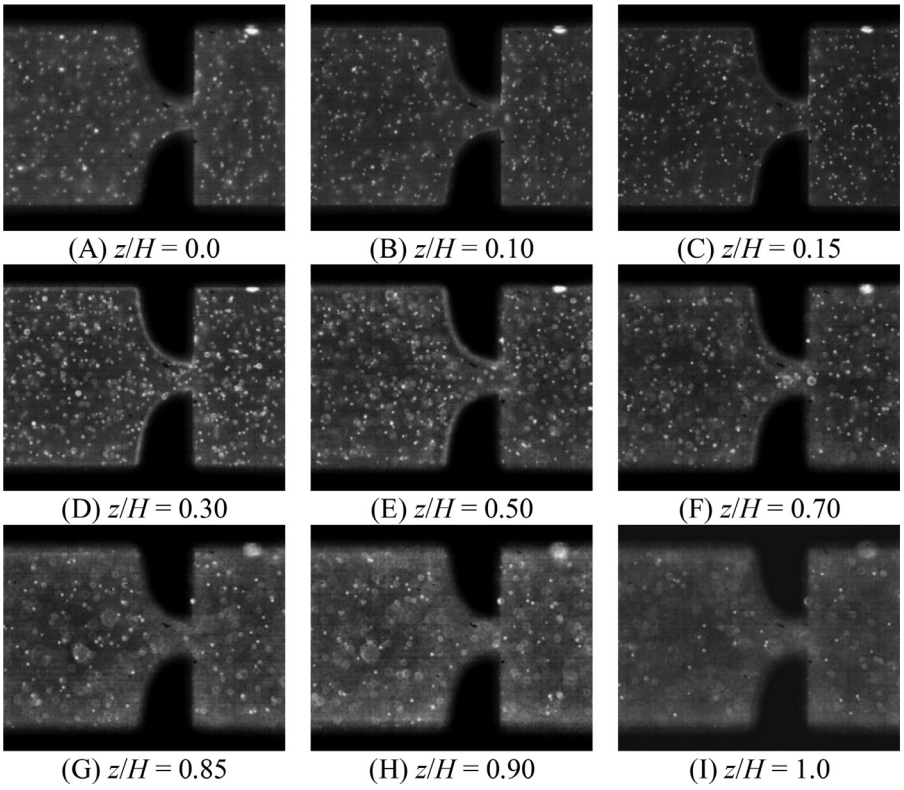

Fig. A.1. Snapshots at several depths of the microchannel filled with fluid and TPs, under no flow conditions, starting from the lower wall at $z/H = 0$ (A) up to the upper wall at $z/H = 1$ (I) in microchannel H_2–f.

Appendix B

In a straight rectangular microchannel, electro-osmotic flow results in a plug-like velocity profile both across the width and depth of the microchannel, i.e., outside the EDLs the velocity is nearly uniform [35,36]. Here, we investigate numerically and experimentally the centerline velocity profile at various depths (z). For microchannels H_2–f and H_3–f, this can be confirmed using numerical simulations of pure electro-osmotic Newtonian flows, by imposing ΔV=30V in microchannel H_2–f and ΔV=20V in microchannel H_3–f, respectively. Fig. B.1 compares the streamwise variation of the centerline (y=0) velocity computed for a 2D channel, as well as for a three-dimensional (3D) channel at several depths: $z/H = \{0.0, 0.05, 0.2, 0.3, 0.5\}$, where the bottom and top walls are located at $z/H = 0$ and 1, respectively. The velocity profiles show a similar behavior at different depths, except near the walls where they approach zero due to the no-slip boundary condition.

To compare with the numerically predicted profiles of the centerline velocity of Fig. B.1, it is instructive to carry out a similar experimental analysis. Accordingly, streamwise profiles of the centerline velocity were measured at several depths, $z/H = \{0.05, 0.15, 0.30, 0.50, 0.70, 0.85, 0.95\}$, and the results are shown in Fig. B.2 for microchannel H_2-f at ΔV=30 V. These profiles are plotted in dimensional form in Fig. B.2-(A), whereas in Fig. B.2-(B) each profile is normalized by the maximum velocity (u_{max}) and compared with the computed profile assumed 2D flow. As shown in Fig. B.2-(B), the normalized experimental and numerical data match well, as expected. In any case, since at z/H=0.15 the velocity profile is identical to that at z/H=0.5, but was much easier to measure, the depth z/H=0.15 was chosen as the default measuring depth for all subsequent measurements with Newtonian fluid, unless otherwise stated.

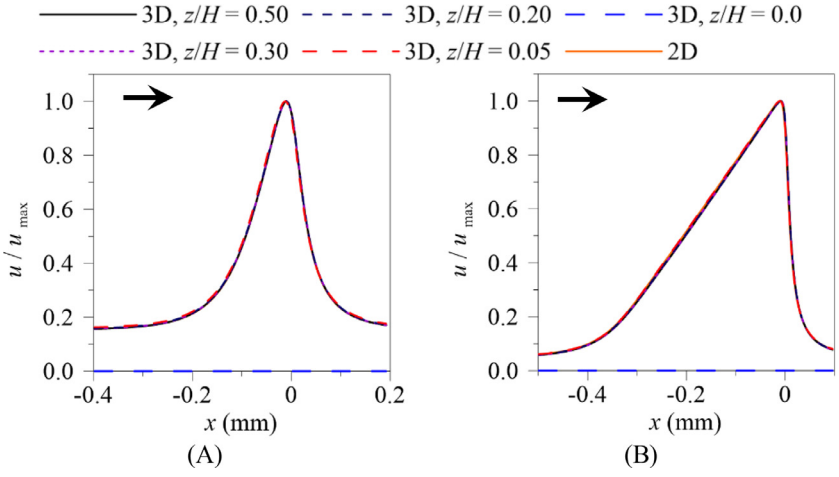

Fig. B.1. Effect of the depth on the normalized centerline velocity profiles (y=0), obtained through numerically computation of 2D and 3D flows at several depths; $z/H = \{0.0, 0.05, 0.2, 0.3, 0.5\}$, assuming a purely EOF of a Newtonian fluid in (A) microchannel H_2–f at ΔV=30 V, and (C) microchannel H_3–f at ΔV=20 V. The black arrows indicate the flow direction.

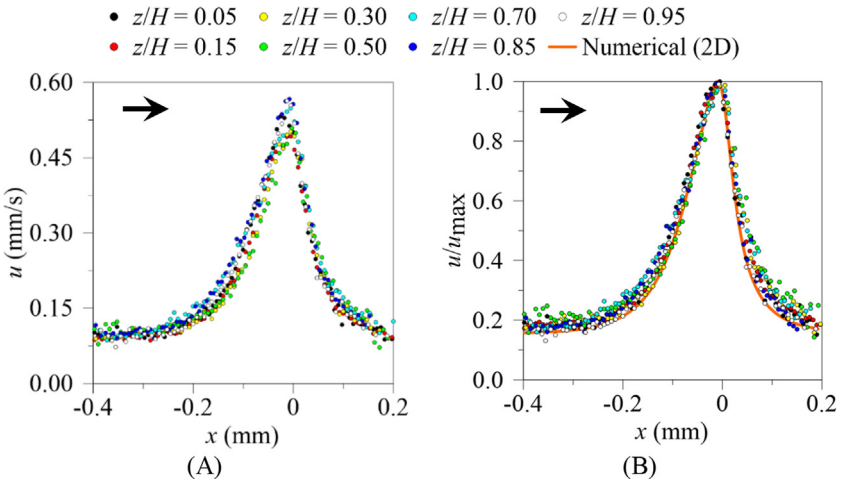

Fig. B.2. Centerline velocity profiles measured at several depths (A) z/H = { 0.05, 0.15, 0.30, 0.50, 0.70, 0.85, 0.95 }, and (B) corresponding normalized velocity profiles for each curve and comparison with the velocity profile computed numerically for 2D flow, in microchannel H_2−f at ΔV=30 V. The black arrows indicate the flow direction.

Appendix C

A small amount of fluorescent dye was added to improve the image quality up to the highest flow rate that can be reached for each microchannel. Fig. C.1 presents the dye effect on the measured centerline velocity profiles for ΔV=5, 10, 30 and 60 V. Fig. C.1-(A) shows a significant difference between the velocity curves measured with and without dye, especially near the throat, with the curves with dye exhibiting higher velocities. A slight shape difference is also observed in Fig. C.1-(B) between the sets of normalized velocity curves with and without dye, with the corresponding 2D numerical prediction standing in between the two experimental sets, suggesting that the dye changes the zeta-potential of the PDMS walls, which consequently changes the EOF velocity through the microchannel. In fact, as shown in Fig. C.2, the use of dye increases the measured velocity by about 25 % along the microchannel centerline, both upstream (Fig. C.2-(A)), and at the throat region (Fig. C.2-(B)). This is why it is important to avoid the addition of dye when studying viscoelastic fluid flows in order to eliminate any potential influence in the flow field which could be amplified in an unknown way by fluid elasticity.

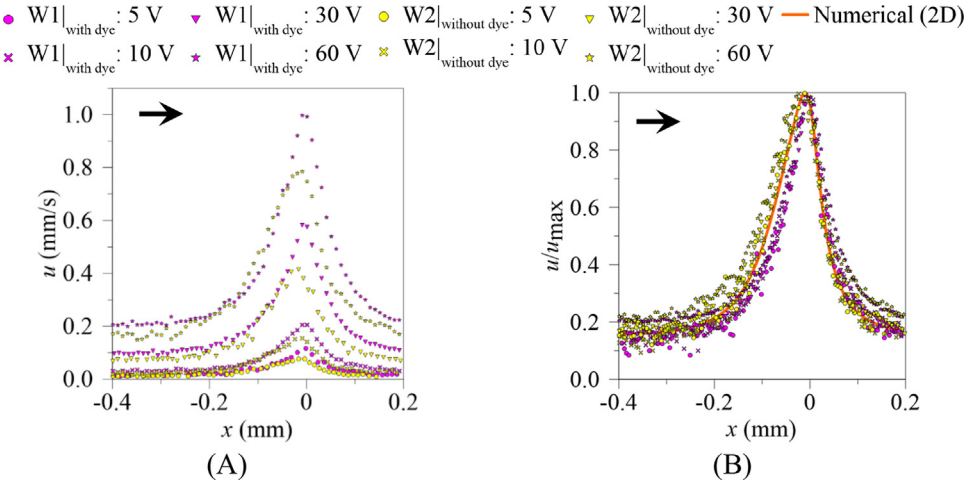

Fig. C.1. Centerline velocity profiles measured at z/H = 0.15 in microchannel H_2−f (W1 with dye and W2 without dye, each measurement was done in a new microchannel) using the 1mM borate buffer, for ΔV=5, 10, 30 and 60V (A), and (B) corresponding normalized velocity profiles and comparison with the velocity profile computed numerically for 2D flow. The black arrows indicate the flow direction.

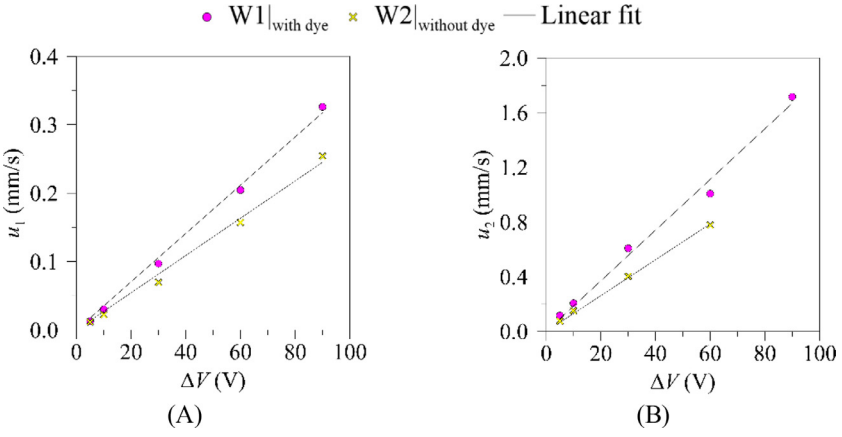

Fig. C.2. Velocity (u_1) at the upstream channel (A) and maximum velocity (u_2) at the throat of the contraction (B) in microchannel H_2−f, using the 1mM borate buffer with (W1) and without dye (W2).

References

[1] N.-T. Nguyen, Z. Wu, Micromixers—a review, J. Micromech. Microeng. 15 (2) (2005) R1–R16.
[2] A.M. Afonso, F.T. Pinho, M.A. Alves, Electro-osmosis of viscoelastic fluids and prediction of electro-elastic flow instabilities in a cross slot using a finite-volume method, J. Non Newtonian Fluid Mech. 179–180 (2012) 55–68.
[3] R.M. Bryce, M.R. Freeman, Abatement of mixing in shear-free elongationally unstable viscoelastic microflows, Lab Chip 10 (11) (2010) 1436–1441.
[4] R.M. Bryce, M.R. Freeman, Extensional instability in electro-osmotic microflows of polymer solutions, Phys. Rev. E 81 (3 Pt 2) (2010) 036328.
[5] M.H. Oddy, J.G. Santiago, J.C. Mikkelsen, Electrokinetic instability micromixing, Anal. Chem. 73 (24) (2001) 5822–5832.
[6] L. Winjet, K.F. Yarn, M.H. Shih, K.C. Yu, Microfluidic mixing utilizing electrokinetic instability stirred by electric potential perturbations in a glass microchannel, Optoelectron. Adv. Mater.-Rapid Commun. 2 (2) (2008) 117–125.
[7] H. Hu, Z. Jin, A. Dawoud, R. Jankowiak, Fluid mixing control inside a Y-shaped microchannel by using electrokinetic instability, J. Fluid Sci. Technol. 3 (2) (2008) 260–273.
[8] M.Z. Huang, R.J. Yang, C.H. Tai, C.H. Tsai, L.M. Fu, Application of electrokinetic instability flow for enhanced micromixing in cross-shaped microchannel, Biomed. Microdev. 8 (4) (2006) 309–315.
[9] Z.Y. Jin, H. Hu, Mixing enhancement by utilizing electrokinetic instability in different Y-shaped microchannels, J. Visualization 13 (3) (2010) 229–239.
[10] R. Poole, M. Alves, P. Oliveira, Purely elastic flow asymmetries, Phys. Rev. Lett. 99 (16) (2007).
[11] P.E. Arratia, C.C. Thomas, J. Diorio, J.P. Gollub, Elastic instabilities of polymer solutions in cross-channel flow, Phys. Rev. Lett. 96 (14) (2006) 144502.
[12] M.S.N. Oliveira, F.T. Pinho, R.J. Poole, P.J. Oliveira, M.A. Alves, Purely elastic flow asymmetries in flow-focusing devices, J. Non Newtonian Fluid Mech. 160 (1) (2009) 31–39.
[13] M.S.N. Oliveira, F.T. Pinho, M.A. Alves, Extensional flow of Newtonian and Boger fluids through a flow focusing microdevice, in: 3rd Micro and Nano Flows Conference, Brunel University, Thessaloniki, Greece, 2011.
[14] F.J. Galindo-Rosales, L. Campo-Deaño, P.C. Sousa, V.M. Ribeiro, M.S.N. Oliveira, M.A. Alves, F.T. Pinho, Viscoelastic instabilities in micro-scale flows, Exp. Therm. Fluid Sci. 59 (2014) 128–139.
[15] S.K. Mitra, S. Chakraborty, Microfluidics and Nanofluidics Handbook: Fabrication, Implementation, and Applications, CRC Press, Boca Raton, Florida, 2011.
[16] P. Pakdel, G.H. McKinley, Elastic instability and curved streamlines, Phys. Rev. Lett. 77 (12) (1996) 2459–2462.
[17] C.-H. Ko, D. Li, A. Malekanfard, Y.-N. Wang, L.-M. Fu, X. Xuan, Electroosmotic flow of non-Newtonian fluids in a constriction microchannel, Electrophoresis 40 (10) (2019) 1387–1394.
[18] L. Campo-Deaño, F.J. Galindo-Rosales, F.T. Pinho, M.A. Alves, M.S.N. Oliveira, Flow of low viscosity Boger fluids through a microfluidic hyperbolic contraction, J. Non Newtonian Fluid Mech. 166 (21–22) (2011) 1286–1296.
[19] P.C. Sousa, F.T. Pinho, M.S. Oliveira, M.A. Alves, Extensional flow of blood analog solutions in microfluidic devices, Biomicrofluidics 5 (2011) 14108.
[20] F. Pimenta, M.A. Alves, Stabilization of an open-source finite-volume solver for viscoelastic fluid flows, J. Non Newtonian Fluid Mech. 239 (2017) 85–104.
[21] F. Pimenta, M.A. Alves, Electro-elastic instabilities in cross-shaped microchannels, J. Non Newtonian Fluid Mech. 259 (2018) 61–77.
[22] M.S.N. Oliveira, M.A. Alves, F.T. Pinho, G.H. McKinley, Viscous flow through microfabricated hyperbolic contractions, Exp. Fluids 43 (2–3) (2007) 437–451.
[23] P.C. Sousa, E.J. Vega, R.G. Sousa, J.M. Montanero, M.A. Alves, Measurement of relaxation times in extensional flow of weakly viscoelastic polymer solutions, Rheol. Acta 56 (1) (2017) 11–20.
[24] I.F. Sbalzarini, P. Koumoutsakos, Feature point tracking and trajectory analysis for video imaging in cell biology, J. Struct. Biol. 151 (2) (2005) 182–195.
[25] K. Zografos, F. Pimenta, M.A. Alves, M.S. Oliveira, Microfluidic converging/diverging channels optimised for homogeneous extensional deformation, Biomicrofluidics 10 (4) (2016) 043508.
[26] P.C. Sousa, I.S. Pinho, F.T. Pinho, M.S.N. Oliveira, M.A. Alves, Flow of a blood analogue solution through microfabricated hyperbolic contractions, in: J.M.R.S. Tavares, R.M.N. Jorge (Eds.), Computational Vision and Medical Image Processing: Recent Trends, Springer, Netherlands, Dordrecht, 2011, pp. 265–279.
[27] P.C. Sousa, F.T. Pinho, M.S.N. Oliveira, M.A. Alves, Efficient microfluidic rectifiers for viscoelastic fluid flow, J. Non Newtonian Fluid Mech. 165 (11) (2010) 652–671.
[28] J.M. Dealy, Weissenberg and Deborah numbers - their definition and use, Rheol. Bull. 79 (2) (2010) 14–18.
[29] S.H. Sadek, F. Pimenta, F.T. Pinho, M.A. Alves, Measurement of electroosmotic and electrophoretic velocities using pulsed and sinusoidal electric fields, Electrophoresis 38 (7) (2017) 1022–1037.
[30] R.M. Matos, M.A. Alves, F.T. Pinho, Instabilities in micro-contraction flows of semi-dilute CTAB and CPyCl solutions: rheology and flow instabilities, Exp. Fluids 60 (9) (2019) 145.
[31] M.S.N. Oliveira, P.J. Oliveira, F.T. Pinho, M.A. Alves, "Effect of contraction ratio upon viscoelastic flow in contractions: the axisymmetric case, J. Non Newtonian Fluid Mech. 147 (1–2) (2007) 92–108.
[32] H. Bruus, Theoretical Microfluidics, Oxford University Press Inc, Oxford, UK, 2008.
[33] S.J. Haward, M.S.N. Oliveira, M.A. Alves, G.H. McKinley, Optimized cross-slot flow geometry for microfluidic extensional rheometry, Phys. Rev. Lett. 109 (12) (2012) 128301.
[34] S.J. Haward, Microfluidic extensional rheometry using stagnation point flow, Biomicrofluidics 10 (4) (2016) 043401.
[35] R.J. Yang, L.M. Fu, Y.C. Lin, Electroosmotic flow in microchannels, J. Colloid Interface Sci. 239 (1) (2001) 98–105.
[36] M. Pribyl, D. Snita, M. Marek, Multiphysical Modeling of DC and AC Electroosmosis in Micro- and Nanosystems, in: G. Petrone, G. Cammarata (Eds.), Recent Advances in Modelling and Simulation, I-Tech Education and Publishing, Vienna, Austria, 2008, pp. 501–522.